

1
2
3
4
5
6
7
8
9
10
11
12
13
14
15

Global Radiative Flux Profile Dataset: Revised and Extended

Yuanchong Zhang^{1,2}, and William B. Rossow³

¹ Business Integra, Inc. 2880 Broadway, New York, NY 10025, USA.

² NASA Goddard Institute for Space Studies, 2880 Broadway, New York, NY 10025, USA.

³ Franklin, New York.

Corresponding author: Yuanchong Zhang (yz7@columbia.edu)

Key Points:

- The radiative flux profile data product (called ISCCP-FH) is described. It benefits from the new ISCCP cloud products (called ISCCP-H).
- The product is evaluated against the Clouds and the Earth's Radiant Energy System and the Baseline Surface Radiation Network measurements.
- The long-term variations of TOA, surface and in-atmosphere net fluxes are documented and a possible cloud feedback is investigated.

16 **Abstract**

17 The third generation of the radiative flux profile data product, called ISCCP-FH, is described.
18 The revisions over the previous generation (called ISCCP-FD) include improvements in the radi-
19 ative model representation of gaseous and aerosol effects, as well as a refined statistical model of
20 cloud vertical layer variations with cloud types, and increased spatial resolution. The new prod-
21 uct benefits from the changes in the new H-version of the ISCCP cloud products (called ISCCP-
22 H): higher spatial resolution, revised radiance calibration and treatment of ice clouds, treatment
23 of aerosol effects, and revision of all the ancillary atmosphere and surface property products. The
24 ISCCP-FH product is evaluated against more direct measurements from the Clouds and the
25 Earth's Radiant Energy System and the Baseline Surface Radiation Network products, showing
26 some small, overall reductions in average flux uncertainties; but the main results are similar to
27 ISCCP-FD: the ISCCP-FH uncertainties remain $\lesssim 10 \text{ Wm}^{-2}$ at the top-of-atmosphere (TOA) and
28 $\lesssim 15 \text{ Wm}^{-2}$ at surface for monthly, regional averages. The long-term variations of TOA, surface
29 and in-atmosphere net fluxes are documented and the possible transient cloud feedback implica-
30 tions of a long-term change of clouds are investigated. The cloud and flux variations from 1998
31 to 2012 suggest a positive cloud-radiative feedback on the oceanic circulation and a negative
32 feedback on the atmospheric circulation. This example demonstrates that the ISCCP-FH product
33 can provide useful diagnostic information about weather-to-interannual scale variations of radia-
34 tion induced by changes in cloudiness as well as atmospheric and surface properties.

35

36 **Plain Language Summary**

37 The article describes the updated version of the International Satellite Cloud Climatology Project
38 (ISCCP) radiative profile flux product, ISCCP-FH. This version has several important improve-
39 ments over its previous two versions in its radiation model and input datasets of clouds, aerosol
40 and other atmospheric and surface physical properties as well as ancillary datasets. Its spatial
41 resolution is increased to 110km. It now has uncertainties $\lesssim 10 \text{ Wm}^{-2}$ at the top-of-atmosphere
42 (TOA) and $\lesssim 15 \text{ Wm}^{-2}$ at surface for monthly, regional averages based on validations against the
43 direct observations at TOA and surface, slightly improved over the previous versions. We also
44 describe long-term variations of the radiative energy intensity based on the product and give an
45 example to study cloud-radiation feedback using this product. We expect the new product to be
46 used in climate studies like its previous versions.

47 **1 Introduction**

48 Earth's climate is determined by a long-term, global balance of energy exchanges in the
49 form of radiative fluxes, water phase changes, surface-atmosphere exchanges, and transports by
50 the oceanic and atmospheric circulations; but the circulations and their transports are modified
51 by the short-term, local imbalances of the energy and water exchanges. The atmospheric circula-
52 tions (weather) produce water phase changes in the form of clouds and precipitation that feed-
53 back on all of these exchanges and circulation transports. The early focus of weather studies was
54 on the precipitation produced from clouds. The early focus of climate studies was on the modula-
55 tion of the top-of-atmosphere (TOA) radiative fluxes by cloud variations, usually the global av-
56 erage changes that are associated with global mean surface temperature changes. However the
57 global mean temperature is not simply related to the average energy balance because changes in
58 the atmospheric and oceanic circulation redistribute the energy, complicated by induced cloud

59 feedbacks on these circulations. Hence, fully diagnosing cloud-radiative feedbacks on weather
60 and climate requires decomposing the space-time variations of TOA fluxes into surface (SRF)
61 net fluxes that affect the ocean circulation and atmospheric (ATM) net flux profiles that affect
62 the atmospheric motions and cloud (and precipitation) formation. Since the solar (shortwave,
63 SW) fluxes act primarily on the surface and the terrestrial (longwave, LW) fluxes act primarily
64 on the atmosphere, these have to be diagnosed separately. This diagnosis has to be done across a
65 range of space-time scales to establish the coupling at different scales of atmosphere-ocean mo-
66 tions.

67 Obtaining global observations that directly resolve bulk-cloud-process-scale variations of
68 surface fluxes and atmospheric profiles of radiation is infeasible, so another approach is to meas-
69 ure the space-time-resolved variations of the properties of the clouds, atmosphere and the surface
70 and then calculate the radiative fluxes with a detailed radiative transfer model. Atmospheric radi-
71 ative transfer is sufficiently advanced that the accuracy of such calculations is primarily limited
72 by the accuracy and completeness of the description of the cloud, atmosphere and surface prop-
73 erties input to the model. The knowledge and accuracy of this information has increased over the
74 past few decades so that such calculations can improve to reliably reveal more detailed radiative
75 exchanges and their variations. The advantage of the flux-calculation analysis is that determining
76 the causes of flux variations is direct. The success of this approach depends on assessment of the
77 accuracy of the input quantities against independent measurements and verification of the output
78 fluxes against direct measurements.

79 This paper summarizes continuing work along these lines by describing a new data prod-
80 uct, called ISCCP-FH, providing radiative flux profiles at 1°-equivalent-equal-area (approximate-
81 ly 110 km), 3-hr intervals, covering the whole globe for 35 years (see details in Zhang, 2017).
82 This product is a revision of previous versions based on earlier ISCCP data products (Zhang et
83 al., 1995, Rossow and Zhang, 1995, Zhang et al., 2004). The new flux profiles are based on the
84 new ISCCP-H cloud and atmosphere products (Young et al., 2018; Rossow et al., 2022) using a
85 revised radiative transfer model with a refined statistical model of cloud vertical structure. The
86 changes to the radiative transfer model and the input data are described in Sections 2 and 3, re-
87 spectively. The resulting products are described and evaluated compared with more direct meas-
88 urements of surface and top-of-atmosphere fluxes in Section 4. Some basic results and the long-
89 term variations in the fluxes, especially the partitioning of the TOA fluxes into SRF and ATM
90 net fluxes and their average latitude variations, are summarized in Section 5. Section 6 discusses
91 some possible implications for cloud-radiative feedbacks on atmosphere-ocean circulations of
92 one example of cloud-induced changes in the net flux distributions. In conclusion Section 7 con-
93 sideres the state-of-art and suggests other diagnostic studies that can be done with this data prod-
94 uct.

95 **2 Changes in the radiative model**

96 The radiative transfer model used for FH is a further revision of the model used for the
97 two previous versions (FC and FD) and is equivalent to the current radiation code of ModelE2.1
98 of the NASA Goddard Institute for Space Studies (GISS) climate model (Kelly et al., 2020). De-
99 tails of the model's physics are summarized in Zhang (2017), but an even more detailed descrip-
100 tion is in Zhang et al. (2004), especially Table 2. Basic features are (1) use of the correlated-k
101 distribution to integrate over wavelength accounting for absorption and scattering in a vertically
102 inhomogeneous atmosphere, (2) use of a single-Gauss point representation of the angular de-

103 ppendence of radiation, especially of solar radiation, (3) detailed microphysical and optical mod-
104 els of liquid and ice clouds as well as a variety of aerosols, (4) a treatment of the effects of small
105 scale spatial inhomogeneity of clouds, (5) adjustable model levels to coincide with cloud top and
106 bottom boundaries, where physically thicker clouds are divided into smaller layers, (6) spectrally
107 dependent surface albedo and infrared emissivity by surface type, and (7) an angle-dependent
108 ocean reflectivity model that accounts for wind-driven foam. The only revisions of the radi-
109 ative transfer model for calculating the flux profiles from the previous version (see Zhang et al.,
110 2004 for details) are: (1) reformulation of the SW line absorption for H₂O, O₂, CO₂, CH₄, N₂O,
111 etc., using the HITRAN2012 atlas (Rothman et al., 2013) with added weak-SW-absorption val-
112 ues for H₂O, O₂ and CO₂ to eliminate an underestimate of atmospheric gas absorption (Oreo-
113 poulos et al., 2012), (2) improved LW modeling of the H₂O continuum, CFC absorption cross-
114 sections, SO₂ line absorption, and CH₄ and N₂O overlap, especially in polar conditions, (3) re-
115 fined LW treatment for large water vapor amounts (e.g., DeAngelis et al., 2015), including ac-
116 counting for within-layer water vapor gradients, and (4) increased base number of vertical layers
117 from 24 to 43 for LW flux calculation. The code has an estimated accuracy of 1 Wm⁻² for net
118 LW fluxes throughout the troposphere and most of the stratosphere and close to 1% for SW flux-
119 es as compared with line-by-line calculations (cf. Lacis and Oinas, 1991). For ISCCP-FH pro-
120 duction, the monthly-mean aerosol data in the model is replaced by the MAC-v2 global dataset
121 over all years (Kinne, 2019) for better treatment of the spectral details of stratospheric and tropo-
122 spheric aerosol scattering and absorption and for consistency with the ISCCP-H cloud and sur-
123 face retrievals (see Zhang et al., 2010, for sensitivity study of the effect of aerosol uncertainties
124 on surface SW fluxes). Daily total solar irradiance (TSI) is changed to the Solar Radiation and
125 Climate Experiment (SORCE, V-15) based dataset, which is equivalent to that used in the
126 CERES products. Other changes of input parameters are based on the ISCCP-H data product as
127 described in the next section. The FH horizontal resolution is increased from FD to 1°-
128 equivalent-equal-area (approximately 110 km scale) for consistency with the ISCCP-H cloud and
129 ancillary data products. Features of the FH flux calculations that remain unchanged from the FD
130 version (Zhang et al., 2004) are not considered here.

131

132 **3 Changes in input dataset**

133

134 Notable changes to produce ISCCP-H (Rossow, 2017; Young et al., 2018; Rossow et al.,
135 2022), now covering 1983-2018, are: (1) refinements of cloud microphysical models, (2) intro-
136 duction in the retrieval of finite cloud layer thicknesses that increase from the surface to the
137 tropopause, (3) change of the ratio of ice and liquid cloud amounts from 0.96 to 0.64 by lowering
138 the threshold temperature to 253 K, (4) a reduction of total cloud amount (CA) over high topog-
139 raphy ice sheets in summer by about 0.10 (the only significant change) with a shift to more cirrus
140 over both poles (polar cloud changes and evaluations are specifically discussed in Rossow et al.,
141 2022), (5) placement of very thin cirrus at the tropopause instead above it, (6) treatment of strat-
142 ospheric and tropospheric aerosol radiative effects in the cloud and surface retrievals, (7) treat-
143 ment of surface temperature inversions and retrieval of physical surface temperatures (with cor-
144 rection of extreme values), and (8) 1°-equivalent-equal-area mapping of satellite pixels (~ 5 km)
145 sampled at 10 km intervals. Unlike ISCCP-D, ISCCP-H reports the interpolated amounts of the
146 18 cloud types (defined by top pressure, optical thickness and phase) over nighttime periods (ex-
147 cept in winter polar regions). However, as with the FD products, the FH calculations need the
148 full day and night time cloud properties of all the types (top temperature, optical thickness) in

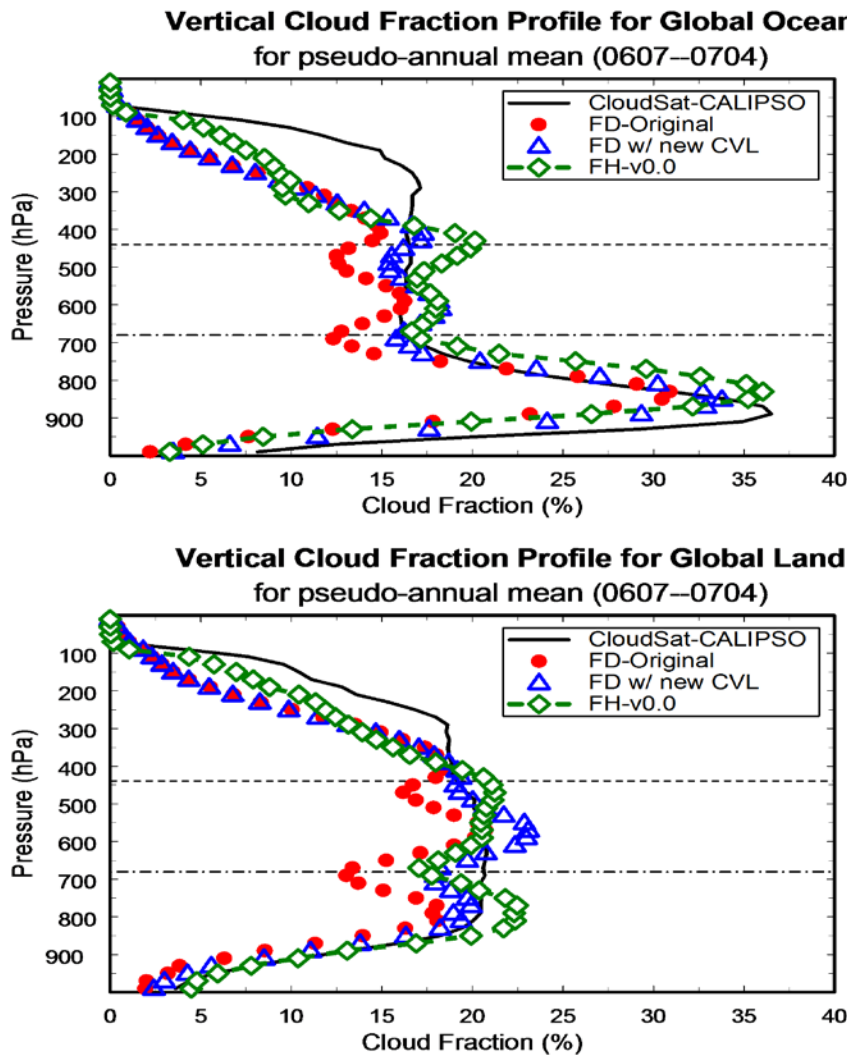
149 addition to their amounts. For most locations, the interpolation is between the nearest in time of
150 before and after daytime results for each nighttime interval. For some locations where there is
151 missing data and for the winter polar regions, the filling involves monthly diurnal averages from
152 three years of data centered on each particular year, supplemented by long-term climatology (see
153 Fig. 1a in Zhang 2017). The filling procedure provides complete cloud type properties over the
154 whole global, every 3 hours.

155

156 All new ancillary inputs for FH (land-water mask, topography, sea ice and snow cover,
157 total ozone abundance, stratospheric and tropospheric aerosol properties, atmospheric profiles of
158 temperature and relative humidity) come from ISCCP-H on the same map grid (Young et al.,
159 2018). These datasets have higher space-time resolutions than before and are more homogeneous
160 over their records (see evaluations of the accuracy of the new ancillary products in Rossow, 2017). In
161 particular, the atmospheric dataset (called NNHIIRS) provides global 3-hr temperature-relative humidity
162 profiles at 16 atmospheric levels with surface temperature inversions.

163

164 Gas abundances (except for water vapor and ozone) are specified as in the GISS climate
165 model, including positive trends in CO₂ and CH₄ abundances from observations (e.g., Hansen et
166 al., 1988; the most up-to-date trends can be found in “Forcings in GISS Climate Model” at
167 <https://data.giss.nasa.gov/modelforce/ghgases/>). Surface albedos (except for water) are derived
168 from an aerosol-corrected surface visible reflectance from ISCCP-H and a 6-band spectral de-
169 pendence model (following Zhang et al., 2004, 2007) for different surface types (although the
170 surface reflectances in ISCCP-H in the visible have been corrected for stratospheric and tropo-
171 spheric aerosol scattering/absorption using MAC-v1, Kinne et al., 2013, the adjustment in FH is
172 done using the full spectral dependence of a later version of the aerosol product, MAC-v2, Kinne
173 et al., 2019). Surface temperatures from ISCCP-H are physical values obtained using estimated
174 narrowband emissivities (at ~11 μm wavelength) by surface type (Rossow, 2017); broadband
175 emissivities by surface type are used in FH calculations (Zhang et al., 2007). The diurnal varia-
176 tions of surface air and skin temperatures from ISCCP-H (which are clear-sky biased) are cor-
177 rected for cloud effects (Zhang et al., 2006).



178

179 **Figure 1.** Global mean cloud amounts (%) at each pressure (hPa) averaged over four mid-season
 180 months in 2007 (pseudo-annual mean) over ocean (upper panel) and land (lower panel) from
 181 CloudSat-CALIPSO (solid black line), the original profile used for ISCCP-FD (red dots), the
 182 profile produced by the refined cloud vertical layer model (CVL) applied to ISCCP-D cloudiness
 183 (blue triangles), and applied to ISCCP-H cloudiness (green diamonds) as used in ISCCP-FH. The
 184 horizontal dashed black lines indicate the pressure boundaries separating low, middle and high
 185 cloud tops.

186

187 A cloud vertical layer (CVL) model accounts for cloud layer overlap in our profile calcu-
 188 lations by assigning specific layer structures to each of the ISCCP cloud types that are defined by

189 three intervals of cloud top pressure, three intervals of optical thickness and phase (including in-
190 terpolated values over nighttime and in winter polar conditions). In each map cell at each time,
191 radiative flux profiles are calculated for each individual layer structure that is present, as well as
192 clear sky (even when not present), and then these are averaged with area-fraction weights to give
193 one flux profile. The original CVL model (Rossow et al., 2005), used for FD (Zhang et al., 2004,
194 Table 5), was based on ISCCP-D and a cloud layer climatology derived from radiosonde humidity
195 profiles (Wang et al., 2000) and later evaluated against CloudSat-CALIPSO profiles (Rossow
196 and Zhang, 2010). Table 3 in Rossow and Zhang (2010) showed excellent statistical agreement
197 between that model and the radar-lidar profiles and Figs. 5 and 6 in that paper show the mean
198 latitude dependence of cloud profiles over ocean and land. The one notable discrepancy was that
199 there was much more single-layer low cloud in that version of CloudSat-CALIPSO that was
200 identified by ISCCP-D as clear sky, but this discrepancy was much reduced in a later version of
201 the lidar analysis that resolved confusion between aerosols and cloud (Mace and Zhang, 2014).
202 Although the assignment of layer structures to the ISCCP cloud types remains the same for FH
203 as in FD, the resulting vertical distribution is slightly changed by revision of the layer position
204 for obscured clouds and the thickness climatology (varying by cloud optical thickness, lati-
205 tude/longitude, month-of-year, ocean/land) based on CloudSat-CALIPSO 2B-GEOPROF-
206 LIDAR (P2_R04, henceforth RL-GEOPROF).

207

208 The refined statistical CVL model used in FH is illustrated in Fig. 1 compared with the
209 older model and with RL-GEOPROF (P2_R04 – this is the 1/3 km lidar version). This version of
210 GeoProf uses Version 3 of the CALIPSO products that made significant changes in the amount
211 of low cloud relative to the earlier version (Mace and Zhang, 2014); however Version 4 of
212 CALIPSO makes more changes, including in the amount of upper troposphere cloud (Liu et al.,
213 2019). Also shown is the refined CVL model applied to ISCCP-D clouds. Although the FH CVL
214 model makes adjustments of the ISCCP cloud distribution (see Zhang et al., 2004) to increase
215 low cloud amount to account for higher-layer-obscuration and to increase thin high-level cloud
216 amount to account for misplacement of some of these clouds to lower levels, the new result still
217 underestimates cloud amount at the highest levels in general by about 0.05-0.10. Some of the un-
218 derestimate of high cloud amount is caused by missed detections of very thin clouds
219 (Stubenrauch et al., 2012, 2013), some by misplacement of thin clouds overlapping lower level
220 clouds (Jin and Rossow, 1997) and some by the fact that the radiative tops for clouds, especially
221 in the tropics, appears lower than the physical top (Liao et al., 1995). The latter two effects may
222 explain the small excess of cloud amount near the 440 hPa level shown in Fig. 1. Low cloud
223 amount over ocean for FH agrees well with RL-GEOPROF but is overestimated by about 0.03
224 over land (given the small changes in the CVL, Figures 5 and 6 in Rossow and Zhang, 2010, still
225 show the zonal monthly mean vertical distribution). The continued refinement of the CloudSat
226 and CALIPSO products (Mace and Zhang 2014, Protat et al., 2014, Liu et al., 2019) makes the
227 magnitude of these differences uncertain. (At the time of writing, the “active release versions for
228 2B-GEOPROF-LIDAR are R04 & R05; P1_R05 is the current version and R04 products will be
229 available until all R05 products have been released,” see
230 <https://www.cloudsat.cira.colostate.edu/data-products/2b-geoprof-lidar>).

231 **4 Product description and evaluation**

232 The FH products report the upward and downward SW and LW fluxes at five levels from
233 the surface to the top-of-atmosphere for "full" sky (actual variable cloud cover), clear sky and
234 overcast sky, as well as the diffuse and direct SW fluxes at the surface. These results are com-
235 piled in five sub-products (all in NetCDF except the last): FH-TOA (radiative fluxes at top of
236 atmosphere with relevant physical quantities, 23 variables), FH-SRF (radiative fluxes at surface
237 with relevant physical quantities, 34 variables), FH-PRF (fluxes at the surface, 680 hPa, 440 hPa,
238 100 hPa, top-of-atmosphere at about 100 km altitude, 91 variables), FH-MPF (monthly average
239 of FH-PRF) and FH-INP (complete inputs up to 355 variables). All of these products are mapped
240 at 1°-equivalent-equal-area and all, except MPF, are reported at 3-hr intervals.

241 Extensive comparisons of the previous versions of this product are the foundation for
242 documenting the small changes/improvements made to the ISCCP-FH products (Zhang et al.,
243 1995; Rossow and Zhang, 1995; Zhang et al., 2004, 2006, 2007, as well as Raschke et al., 2012,
244 2016). Zhang et al. (1995) conducted a complete set of sensitivity studies to determine how un-
245 certainties in the inputs translate to flux uncertainties (still valid for FH), emphasizing the lead-
246 ing importance of clouds for SW fluxes and atmospheric and surface temperatures for LW fluxes.
247 Rossow and Zhang (1995) highlighted the dominance on small space-time scales of sampling
248 differences in comparisons of the calculated fluxes with direct measurements, but also showed
249 that differences in monthly averages better indicated biases in inputs to the calculations. Rossow
250 and Zhang (1995) also conducted a detailed set of comparisons with direct TOA and SRF flux
251 measurements, investigating in particular the effects of differences in space-time sampling and
252 coverage in such comparisons. The mismatch of spatial scales exaggerates the differences for
253 surface flux comparisons by 30-100% because the meteorological conditions do not always
254 match (Rossow and Zhang, 1995; Zhang et al., 2010). The better matching of satellite products
255 contributes less uncertainty. Zhang et al. (2010) also examined the effects of errors in aerosol op-
256 tical depth on the FD-calculated downwelling SW fluxes, motivating the change in the aerosol
257 dataset used for FH. More detailed evaluations of the input quantities, other than clouds, were
258 conducted in Zhang et al. (2006, 2007), which served as the basis for improving the ancillary
259 products, particularly the atmospheric temperature-humidity profiles. Evaluations of the new
260 (non-cloud) inputs for FH are discussed in Rossow (2017) and Rossow et al. (2022). More gen-
261 eral evaluations of the previous flux products, including mapped comparisons and time varia-
262 tions, were made in Rossow and Zhang (1995) and Zhang et al. (2004). Features of the calcula-
263 tions that remain unchanged from FD are not considered here.

264

265

266

267

268

269

270

271 **Table 1.** Differences of monthly mean ISCCP-FH and FD TOA fluxes with CERES (Edition 3A,
 272 CERES Science Team, 2013) and SRF fluxes with BSRN (Ohmura et al., 1998) in Wm^{-2} for
 273 2007. The statistics include spatial variability over location at 110 km scale as well as month-to-
 274 month variability. The uncertainty range is based on the normal deviations (rms with bias re-
 275 moved) (cf. Rossow and Zhang, 1995).

	TOA	
	FH minus CERES	FD minus CERES
SWnet	-7 ± 6	-8 ± 6
Correlation for SWnet	0.99	0.99
LWnet	$+7 \pm 3$	$+3 \pm 3$
Correlation for LWnet	0.99	0.99
Overall uncertainty	≤ 10	≤ 10
	Surface	
	FH minus BSRN	FD minus BSRN
SWnet	-1 ± 15	-4 ± 17
Correlation for SWnet	0.99	0.99
LWnet	-7 ± 12	$+10 \pm 14$
Correlation for LWnet	0.97	0.97
Overall uncertainty	≤ 15	≤ 20

276

277 A summary estimate of the uncertainties of FH and FD fluxes is shown in Table 1 based
 278 on monthly mean comparisons for 2007 at 1° mapping to CERES (SYN1deg Ed3A, see CERES
 279 Science Team, 2013) for TOA fluxes and collocated Baseline Surface Radiation Network stations
 280 (BSRN, Ohmura et al., 1998; Driemel et al., 2018) for SRF fluxes. Comparisons were also made
 281 by Stackhouse et al. (2021) to the latest version of GEWEX-SRB Rel4 (which is also based on
 282 ISCCP-H) with respect to CERES Energy Balanced and Filled (EBAF) Ed4.1 (Loeb et al.,
 283 2018), which is an adjusted version of Ed3A to reduce the original net imbalance of $+4.3 \text{ Wm}^{-2}$
 284 to force agreement with an imbalance estimate of $< 1 \text{ Wm}^{-2}$ from ocean heat measurements
 285 (Loeb et al., 2009). The comparison results from Stackhouse et al. (2021) to a later version of
 286 CERES do not indicate any changes of the comparison statistics for the overall biases (and
 287 standard deviation) shown in Table 1. Raschke et al. (2012, 2016) compare many of these same
 288 products, including ERBE, multiple versions of CERES, BSRN, as well as SRB and ISCCP-FD,
 289 in much more detail.

290 The comparison statistics (much more detail is given in Zhang 2017) indicate that the FH
 291 results are only a very slight improvement over the FD results (Zhang et al., 2004). These statis-
 292 tics encompass both spatial variation of monthly averages over the global (110 km scale) and
 293 month-to-month variations, seasons included. Clear sky SW absorption has increased producing
 294 better agreement with line-by-line calculations (cf. Oreopoulos et al., 2012). As noted below
 295 some changes in surface LW fluxes are associated with the change of atmospheric temperature-
 296 humidity inputs. The changes in ISCCP-H cloud microphysics did not produce notable changes
 297 in the fluxes overall. Although some notable changes of polar cloud properties occurred in IS-
 298 CCP-H (decrease of total cloud amount in southern summer with shift of some remaining clouds
 299 to cirrus category at both poles), the only significant change in the FH polar fluxes is a decrease
 300 of surface LWdn by 10-20% (more in northern winter and southern summer). This decrease is
 301 caused almost entirely by the change of the ancillary atmospheric temperature-humidity dataset

302 from TOVS in FD to NNHIRS in FH. The latter is considerably colder (5-10 K) near the surface
303 (but about the same at higher altitudes) than the former, which was based on a fixed climatology
304 estimated from conventional observations made from 1958-1973. NNHIRS is more consistent
305 with other temperature data (Rossow et al., 2022). All other differences of monthly mean fluxes
306 between FD and FH in the polar regions are $< 10 \text{ Wm}^{-2}$.

307 The dominant source of uncertainty in the flux profiles is still associated with the cloud
308 vertical layer (CVL) model, which is a small improvement over the previous version (Fig. 1).
309 The new model still underestimates cloud amounts near the tropopause (at the 200 hPa level) by
310 about 0.05 (land) and 0.10 (ocean). Based on the GEWEX assessment of ISCCP-D clouds
311 (Stubenrauch et al., 2013), some of these high clouds (about 0.05) are actually missed by ISCCP-
312 D, but they have such low optical thicknesses that the resulting flux biases are estimated to be $<$
313 1 Wm^{-2} (Zhang et al., 2004). Most of the near-tropopause clouds are actually detected but dis-
314 placed to lower levels; as shown by Chen and Rossow (2002), even though these clouds are con-
315 sistent with the narrowband IR radiances, they are below the water vapor emission level at wave-
316 lengths $> 25 \mu\text{m}$, which may account for part of an underestimate of LW emission (LWup) at
317 TOA. The new cloud vertical model also overestimates low-level cloud amount by about 0.03
318 over land but not ocean and top pressure for low clouds by about 75 hPa over oceans., Although
319 Fig. 1 shows an overestimate of low cloud amount over land relative to RL-GEOPROF, the
320 BSRN comparison still indicates a small low bias of LWdn at the surface in FH, associated with
321 the change in atmospheric temperature-humidity profiles. The new product in ISCCP-H
322 (NNHIRS) has near-surface air temperatures within 1-2 K over land compared to surface meas-
323 urements but is drier at the surface over land (Rossow et al., 2022).

324 To estimate the effects on fluxes of uncertainties in the cloud layer amounts, flux profiles
325 were calculated for the middle day of the four mid-season months (January, April, July, October
326 2007) with high cloud amounts (cirrus, cirrostratus, defined by optical thickness < 23) increased
327 or low cloud amounts (all types) decreased as Fig. 1 suggests. Although the input cloud amounts
328 from ISCCP-H were changed globally, the resulting changes at each location and level are lim-
329 ited by the constraint that total cloud amount cannot exceed unity nor can a type of cloud fraction
330 become negative. Hence the global average changes are smaller than some local changes. Since
331 the atmospheric absorption of solar radiation is weak, the SW flux profile is relatively insensitive
332 to the vertical distribution of clouds, especially since the total optical thickness is constrained (cf.
333 Chen et al., 2000). For an increase (decrease) of high (low) global mean cloud amount of about
334 0.05, the global mean SWnet at all levels decreases (increases) by about $6\text{-}7 \text{ Wm}^{-2}$, with a slight-
335 ly larger change near the surface for changing low cloud amount and at mid-levels for changing
336 high cloud amount. Since the total optical thickness is constrained to be the same, most of this
337 change occurs simply because total cloud amount is increased (decreased). Thus uncertainties in
338 the CVL of this magnitude, if constrained by total cloud amount and optical thickness, contribute
339 very little uncertainty in the shape of the SWnet profile (see also Zhang et al., 1995, for sensitivi-
340 ty tests of the effects of uncertainties in total cloud amount and optical thickness). For similar
341 changes in high (low) cloud amounts, the global mean LWnet (which is negative) increases by
342 about $3 \text{ to } 6 \text{ Wm}^{-2}$ going from the surface to TOA for the high cloud increase and decreases by
343 about $1 \text{ to } 3 \text{ Wm}^{-2}$ going from TOA to the surface for the low cloud decrease. Thus, although
344 local effects can be larger, the uncertainty of net fluxes at all levels in the atmosphere is of the
345 same order as the flux uncertainties at TOA and surface shown in Table 1: the total flux profile

346 uncertainties, especially in LW, are larger because of uncertainties in the atmospheric tempera-
 347 ture (and humidity) profile.

348

349 **Table 2.** Evolution of flux biases (Wm^{-2}) from comparisons with spatially matched ERBE or
 350 CERES at top-of-atmosphere and GEBA (Wild *et al.* 2017) or BSRN at surface (Driemel *et al.*
 351 2018)†.

	TOA		
	FC – ERBE	FD – ERBE	FH – CERES
SWup	+10.7	+4.7	+7.2 (+7.5, +5.0)
LWup	-1.1	-2.2	-7.1 (-7.0, -8.0)
Net	-9.3	-2.0	0.0 (-0.5, -3.2)
	Surface		
	FC – GEBA	FD – BSRN	FH – BSRN
SWdn	+15.2	+2.0	-1.4
LWdn	-19.4	+2.2	-7.5
Net	N/A	N/A	(+4.1)

352 †The FC comparisons are based on 16 seasonal months over 1985 – 1989 as reported in Rossow and
 353 Zhang (1995). The FD comparison with ERBE is also based on the same 16 seasonal months as FC but
 354 the FD comparison with BSRN is based on all months over 1992 – 2001 as reported in Zhang *et al.*
 355 (2004). The FH comparisons are based on monthly means in 2007 from CERES (SYN1deg Ed3a) and
 356 BSRN; values in parentheses represent the bias with respect to CERES SYN1deg 4.1 for 2007–2009 pe-
 357 riod and EBAF 4.1 over the 2001–2009 period, respectively, cited from Stackhouse *et al.* (2021).
 358

359 Table 2 shows the evolution of comparison differences for the three versions of these
 360 products (including alternate versions of the CERES products, cf. Stackhouse *et al.*, 2021). The
 361 bias of FH upwelling SW (SWup) flux at TOA with respect to CERES is consistent in sign with
 362 the bias of downwelling SW (SWdn) flux at SRF with respect to BSRN, an improvement over
 363 the FC/FD SW biases that were not consistent at TOA and SRF. The bias of SWdn and LWdn at
 364 SRF is much smaller for FD and FH compared to BSRN than for FC compared to GEBA. The
 365 smaller bias of LWup at TOA in FC/FD when compared with ERBE becomes larger for FH when
 366 compared to CERES, even though the latter flux is smaller than ERBE and the FH flux is smaller
 367 than FC/FD. These differences for FH are still within the uncertainties of the comparison datasets
 368 as discussed next.

369 The changing comparison results in Table 2 can also be related to changes in the datasets
 370 used for evaluation of FC/FD/FH that have their own uncertainties, including uncertainty in cali-
 371 bration, which is smaller for CERES/BSRN than for ERBE/GEBA. Thus, some of the changes
 372 (especially biases) in the comparison results could be caused by changed reference data. In addi-
 373 tion, there are differences in the wavelength ranges defining SW and LW fluxes (measurements
 374 are corrected for limited instrument sensitivity), treatment of angle dependence (measurements
 375 are corrected) and domain area represented (smaller for surface measurements than satellite-
 376 based products).

377 ERBE/CERES separate SW and LW at $5.0 \mu\text{m}$, calibrating to account for instrument sensi-
 378 tivity ranges that do not correspond precisely to this division. The ERBE scanners were sensi-
 379 tive in the (approximate) wavelength range of 0.2 to $4.5 \mu\text{m}$ in the SW and 6 to $35 \mu\text{m}$ in the LW;

380 the ERBE LW is truncated at 50 μm (Barkstrom et al., 1989). The CERES instruments are sensi-
381 tive in the range 0.3 to 5 μm in the SW and 5 to 200 μm in the LW (Loeb et al., 2018), which is
382 determined from a Total channel (0.3 to 200 μm) with a decreasing sensitivity longward of 30
383 μm (Loeb et al., 2001). For surface SW instruments, corrections are needed for the dome trans-
384 mission (estimated at about 0.95) and an uncertain thermal offset; LW instruments have various
385 shortwave cutoffs at 3.5-5.0 μm to exclude sunlight, but there is some thermal radiation in this
386 wavelength range (Kohsiek et al., 2006). Philipona et al. (2001) describe the typical wavelength
387 coverage by SW instruments as 0.3-2.8 μm and LW as 4.0-50 μm , with as much as 2% of the LW
388 flux at wavelengths $> 50 \mu\text{m}$; they estimate the resultant flux uncertainties of SW $\pm 5 \text{ Wm}^{-2}$ and
389 LW $\pm 10 \text{ Wm}^{-2}$. FH (as well as FC/FD) includes wavelengths 0.2-15.0 μm in the SW radiation
390 from the sun, but without thermal radiation from Earth, and includes wavelengths 0.2-200 μm in
391 the LW radiation from Earth (for a complete Planck function), but without solar radiation. Effec-
392 tively, however, the calculated fluxes represent 0.2-5.0 μm for SW and 5.0-200 μm for LW.

393 There could also be subtle differences in the treatment of angle dependencies of the direct
394 measurements, which have to be corrected, and the radiative transfer calculations. The satellite
395 radiance measurements are converted to fluxes using empirical angle dependence models that
396 have different but much more detailed scene dependencies for CERES than for ERBE (Loeb et
397 al., 2001; Su et al., 2015a, b). The surface measurements have to be corrected for sensor angle
398 dependence (e.g., Michalsky et al., 1999).

399 The satellite-based flux data products represent larger areas (of order 110 km in size for
400 FH but about 280 km for FC/FD) than the surface measurements (of order 50 km in size), which
401 introduce differences in the presence of incomplete cloud cover (cf. Rossow and Zhang, 1995).
402 The radiative transfer calculations ignore small lateral exchanges (a better approximation at larg-
403 er scales). Zhang et al. (2010) show that simple comparisons of the satellite-based products with
404 surface measurements exhibit significantly larger differences if cloud and atmospheric conditions
405 are not matched: rms differences in SW fluxes decrease by a factor of about two if cloud cover
406 and optical thickness agree and LW flux rms differences decrease by as much as 30% if cloud
407 cover and atmospheric temperature are matched with biases almost eliminated.

408 Another systematic difference is that ERBE/CERES define the top-of-atmosphere to be at
409 30 km and 20 km, respectively (Barkstrom et al., 1989 for ERBE, Loeb et al., 2018 for CERES),
410 whereas FC/FD/FH define top-of-atmosphere at 100km. In FH the average differences in upward
411 fluxes between the 100 hPa level and TOA imply that the flux difference related to this differ-
412 ence in reference level is $< 1 \text{ Wm}^{-2}$ for SW but could be as much as 2-3 Wm^{-2} for LW, which
413 might be part of the lower FH values relative to ERBE/CERES (Table 2).

414 Given the uncertainties of the comparison datasets and the estimates for FH based on pre-
415 vious evaluations, especially the sensitivity tests for the input datasets, the overall uncertainty of
416 the FH fluxes (including the profiles) is in the range between the TOA and surface estimates
417 shown in Table 1, namely about 10-15 W/m^2 for monthly averages at 110 km scale.

418 Table 3 compares the flux results from all three versions as global mean values averaged
419 over the same five year period (mid-seasonal months for April 1985 – January 1989), including
420 Cloud Radiative Effect (CRE, the difference between all-sky and clear-sky fluxes). The system-
421 atic decrease of SWup at TOA and SWdn at SRF, as well as increase of SWnet in ATM, from FC

422 to FD is caused by the added treatment of ice clouds in FD; the changes from FD to FH reflect
 423 the addition of more atmospheric absorption mostly by gases and a little by aerosols. An increase
 424 of surface albedo between FD and FH is related to the added treatment of aerosols in ISCCP-H
 425 and a more detailed climatology in FH. The small decrease in LWup (and increase in LWcre) at
 426 TOA between FD and FH is related to small increases of high-level cloudiness (in FC only the
 427 average cloud top temperature over each map grid domain is used whereas FD and FH determine
 428 fluxes for a distribution of cloud properties within each domain). Despite the elimination of ex-
 429 treme surface temperatures in ISCCP-H (Rossow et al., 2022), SRF LWup increased slightly in
 430 FH compared with FD. Small changes in the treatment of low cloud base estimates in the CVL
 431 from FD to FH, as well as the changes in atmospheric temperature-humidity, caused a decrease
 432 of LWcre at SRF for FH. These small changes in the lower atmosphere clouds and temperature-
 433 humidity changed the sign of the small in-atmosphere LWcre in FH to a small heating effect. In
 434 general, however, the overall changes from FC to FH are relatively small, similar in magnitude
 435 to the estimated uncertainties. The last column in Table 3 summarizes the FH results averaged
 436 over 34 whole years (July 1983 to June 2017), where the standard deviations include both the
 437 spatial variability of monthly mean values in the 1°-equivalent-equal-area mapping and the
 438 month-to-month variations, seasons included. The overall assessment of cloud radiative effects is
 439 that they reduce the heating of Earth at TOA by about 22 Wm^{-2} , which appears as a reduction of
 440 surface heating by about 30 Wm^{-2} but a heating of the atmosphere by 8 Wm^{-2} (cf. Table 2 in
 441 Wild et al., 2018).

442

443 **Table 3.** (First three numerical columns) Comparison of global-time-average flux results for 16
 444 mid-seasonal months for the same four year period (April 1985 to January 1989) from the three
 445 versions of calculations (all are in Wm^{-2} except albedo in %) and (Rightmost column) mean
 446 (standard deviation) of 1°-equal-area maps over all the monthly means from July 1983 to June
 447 2017^a.

448

Quantity	FC	FD	FH	34-year FH
TOA				
SWdn	341.6	341.8	340.3	340.4 (130.9)
SWup	111.5	105.6	104.6	104.5 (50.6)
LWup	234.2	233.2	231.5	232.3 (32.8)
SWnet	230.1	236.3	235.7	236.1 (107.1)
LWnet	-234.2	-233.2	-231.5	-232.3 (32.8)
NET	-4.1	3.1	4.2	3.8 (88.3)
SWcre	-53.7	-50.4	-49.0	-48.8 (33.8)
LWcre	21.3	26.2	28.3	26.9 (15.4)
Albedo	32.6	30.9	30.7	30.7 (13.8)
Atmosphere				
SWnet	65.0	70.8	77.4	77.0 (30.5)
LWnet	-188.4	-182.0	-179.8	-178.9 (37.6)
NET	-123.4	-111.2	-102.5	-101.9 (33.2)
SWcre	-1.6	2.9	2.5	2.6 (3.5)
LWcre	-3.6	-3.1	7.1	5.4 (20.8)
Surface				
SWdn	193.4	189.4	183.4	183.9 (84.2)

SWup	28.3	24.0	25.1	24.8 (35.2)
LWdn	348.3	344.6	346.0	340.9 (76.1)
LWup	394.1	395.7	397.6	394.3 (75.6)
SWnet	165.1	165.4	158.3	159.1 (80.3)
LWnet	-45.8	-51.1	-51.6	-53.4 (25.7)
NET	119.3	114.3	106.7	105.7 (83.5)
SWcre	-52.2	-53.3	-51.5	-51.5 (36.0)
LWcre	24.9	29.3	21.2	21.5 (15.3)
Albedo	14.6	12.7	13.7	13.5 (18.6)

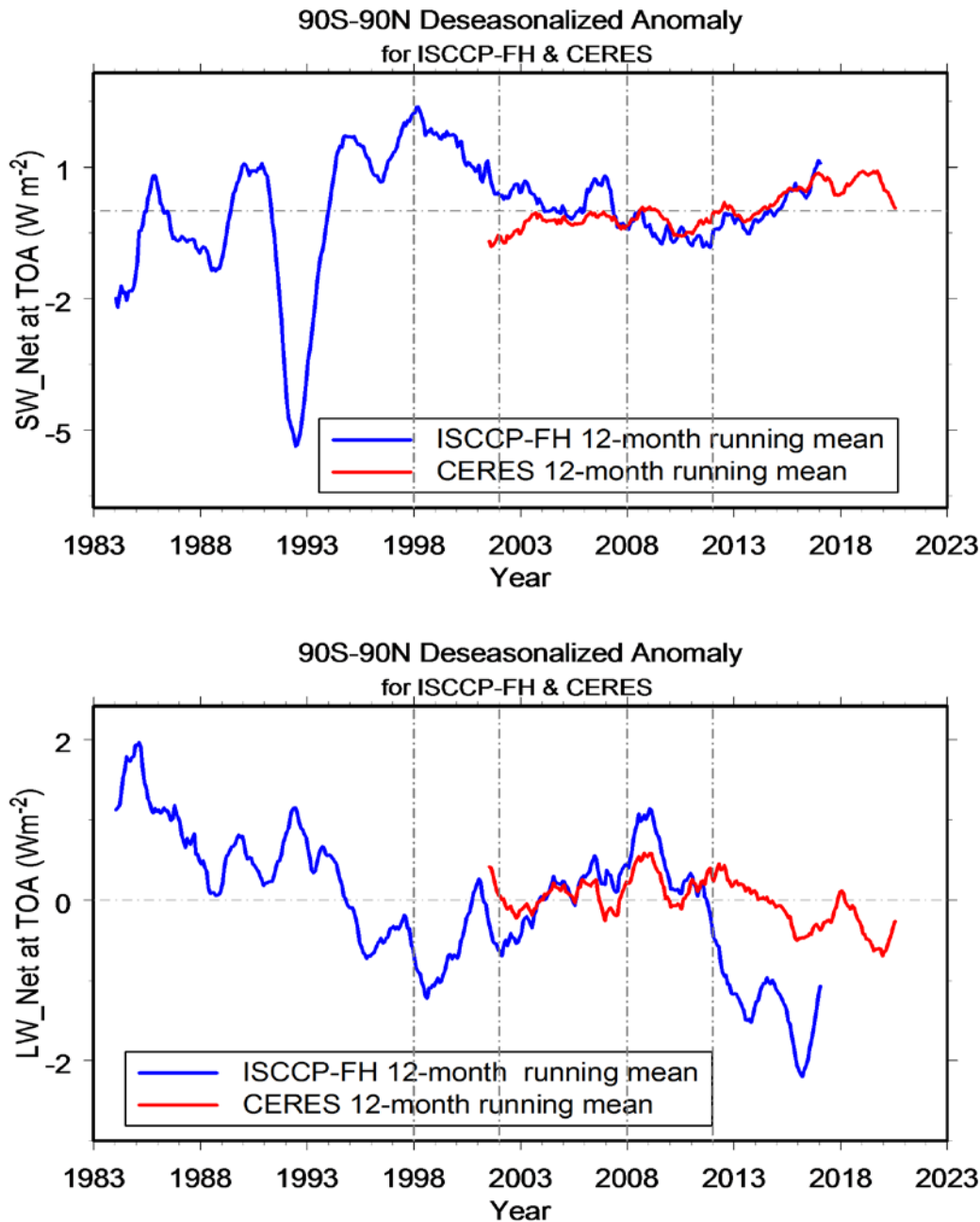
449

450 ^aCloud Radiative Effect (CRE as used in this table in SWcre and LWcre for SW and LW,
 451 respectively) is for net fluxes, positive sign means radiative heating in the system (the earth-
 452 atmosphere, earth or atmosphere system for TOA, surface or atmosphere) as conventionally
 453 defined. The original FH 1°-equal-area map is re-gridded to the same 2.5°-equal-area map as FC
 454 and FD before averaging for the 16-month comparison, but not in the last column. Albedo for
 455 both TOA and SRF are calculated based on averaged SWup and SWdn (because albedo is the
 456 ratio of SWup to SWdn that cannot be linearly averaged); however, the standard deviation for
 457 Albedo is based on all monthly mean albedo values (like all other parameters) for a reference.

458 **5 Some features of the long-term FH record**

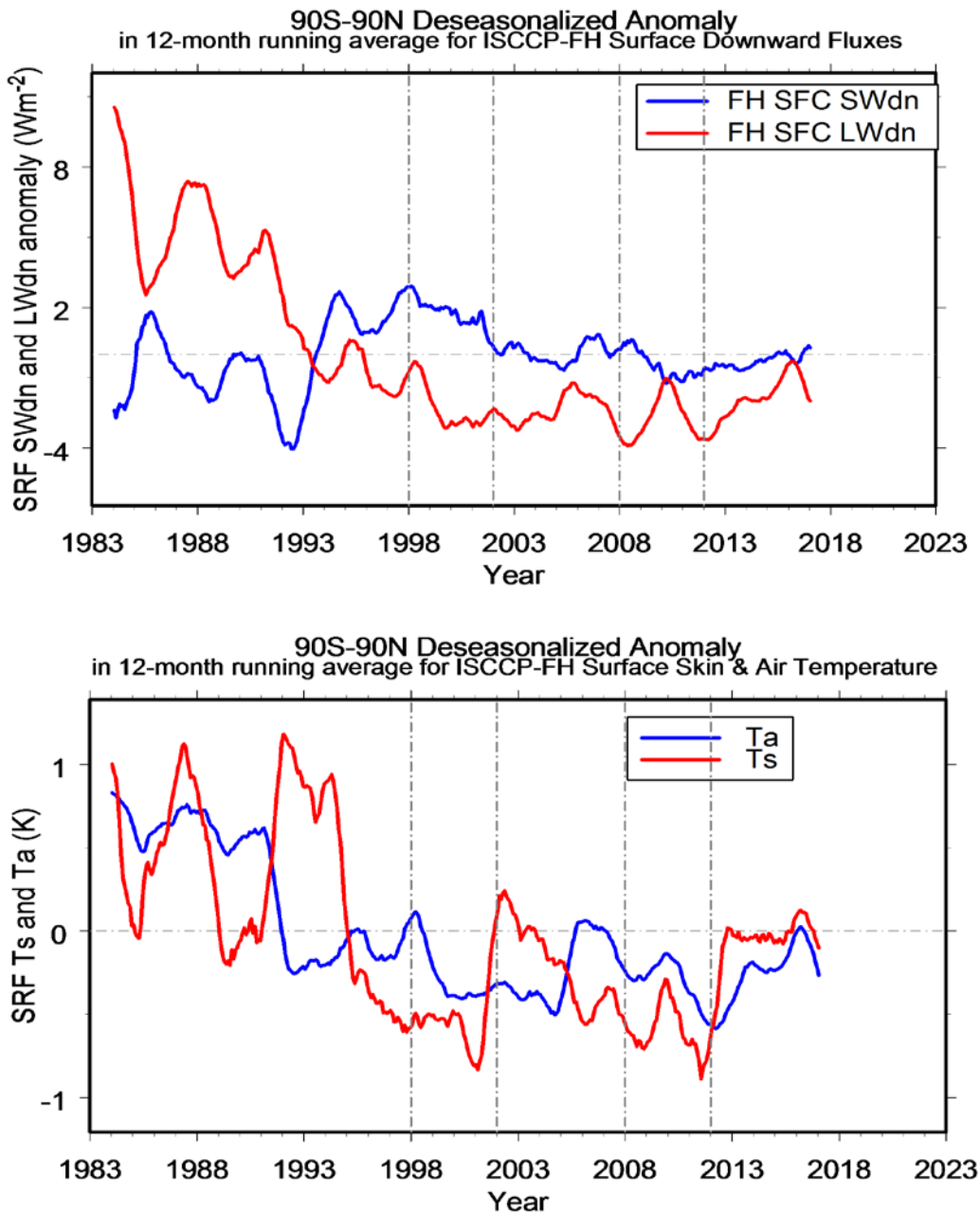
459 Despite the magnitude of the estimated uncertainties of the monthly mean FH fluxes (Ta-
 460 ble 1), the long-term record of global mean net flux anomalies at TOA over about the last 15
 461 years shows agreement within mutual uncertainties with the CERES (SYN1deg Ed4.1) record,
 462 especially in SWnet (Fig. 2) (cf. EBAF Ed4.1 anomalies in Loeb et al., 2021). This comparison
 463 provides an additional evaluation of FH, especially since the anomalies shown are relative to
 464 each datasets own record average. The longer FH record suggests that the recent increase in
 465 SWnet (decreased albedo, see also Goode et al., 2021 and Stephens et al., 2022) may not be a
 466 trend but a long-term variation. However, the magnitude of the recent changes in LWnet in FH
 467 (decreased emission from about 2005 to 2012 and increased emission to 2017) is more than
 468 twice as large as shown in the CERES record. The larger variability in the FH record in the
 469 1980s and 1990s, exclusive of that associated with Pinatubo in 1991-1993, may be related to
 470 more variability in the ISCCP satellite coverage; however Zhang et al. (2004) show that the
 471 monthly average SWup and LWup flux anomalies in the tropics for FD for 1985-1999 agree with
 472 those from the ERBS record (Wielicki et al., 2002; Wong et al., 2006) to within about 1 Wm^{-2}
 473 (correlation about 0.8). Hence, some of the larger LW flux variation may be produced by the at-
 474 mospheric temperature-humidity dataset, rather than the cloud variations.

475



476

477 **Figure 2.** Deseasonalized anomalies (shown as 12-month running averages) of global monthly
 478 mean TOA net fluxes (Wm^{-2}) from FH (blue curves) compared to CERES (SYN1deg Ed4.1, red
 479 curves) for SWnet (upper panel) and LWnet (lower panel) from 1983 to 2019, where FH covers
 480 July 1983 to June 2017 while CERES covers 2001 to 2020. The anomalies for each dataset are
 481 determined relative to their own record averages. Positive SWnet anomaly indicates more ab-
 482 sorption (lower planetary albedo) and positive LWnet anomaly indicates decreased emission.
 483 The vertical lines delineate two time periods (1998-2002, 2008-2012) discussed later.
 484



485
486

487 **Figure 3.** (Upper panel) Deseasonalized anomalies (shown as 12-month running averages) of
 488 global monthly mean downwelling SRF fluxes (Wm^{-2}) from FH for SWdn (blue curve) and
 489 LWdn (red curve). The anomalies for each dataset are determined relative to their own record
 490 averages. (Lower panel) Deseasonalized anomalies (shown as 12-month running averages) of
 491 global monthly mean near-surface air temperature (TA, blue curve) and surface skin temperature
 492 (TS, red curve) in Kelvins from ISCCP-FH. The vertical lines delineate two time periods (1998-
 493 2002, 2008-2012) discussed later.

494 At the surface the global mean downwelling flux anomalies from FH are shown in Fig. 3
495 (upper panel). As discussed in Rossow and Zhang (1995) and Zhang et al. (2010), such compari-
496 sons (with surface station observations) are affected by the point-to-area mismatch of atmospher-
497 ic conditions, so we focus on only the larger scale tendencies. Several analyses of surface meas-
498 urements of SWdn – spatial coverage limited to land stations – have suggested an overall de-
499 crease from about 1960 to about 1990 and an increase afterwards into the early 2000s (Wild et
500 al., 2005, cf. Wild, 2009). An increase after 2000 (to around 2008 and then a second increase af-
501 ter a short decrease) is consistent with the recent changes from CERES (Fig. 2). The FH record
502 for SWdn is qualitatively similar if trend lines are fit to the periods before Pinatubo and after
503 2000, but shows that the peak in the late 1990s is larger than the values after 2005. Pinker et al.
504 (2005) show other similar results based on the ISCCP-D data with an increase from 1983 to
505 about 2001.

506 The LWdn in FH shows a very large anomaly declining rapidly at the beginning of the
507 record until the late 1990s. After that there is an increase by a little less than 2 Wm^{-2} . Stephens et
508 al. (2012) calculate an increasing LWdn under clear conditions over ocean by 3 Wm^{-2} from
509 1988-2008, based on SST, column water vapor and CO₂ abundance determinations. The FH cal-
510 culations (and previous versions) account for increasing CO₂ and CH₄ abundances, which
511 should produce an increase in LWdn, all other things being equal; but as Fig 3 (lower panel)
512 shows, the near-surface air temperature (T_a) and skin temperatures (T_s) from ISCCP-H used in
513 FH are generally decreasing slightly. The magnitude of the decrease over the record is only about
514 1 K (well within the measurement uncertainty), but surface-based temperature records suggest
515 an increase a little less than 1K over this same period (GISTEMP Team, 2021). The air tempera-
516 tures (and humidities not shown) in ISCCP-H and FH show a small downward trend and small (\leq
517 1 K) discontinuities that are related to changes in the NNHIRS temperature and humidity retriev-
518 als between satellites in the HIRS series; this behavior of the HIRS retrievals propagates into the
519 FH LW results. The overall downward trend in FH LWdn at SRF is likely due to the properties of
520 the atmospheric data used in the calculations, but the magnitude of the uncertainties, at least
521 from the 1990s onward, is similar to the estimate shown in Table 1.

522 Overall, while these long-term results from FH might be taken to show good accuracy
523 relative to direct measurements, especially for the SW fluxes, we emphasize that the disagree-
524 ments shown in Figs. 2 and 3 are well within the estimated uncertainties of both datasets.

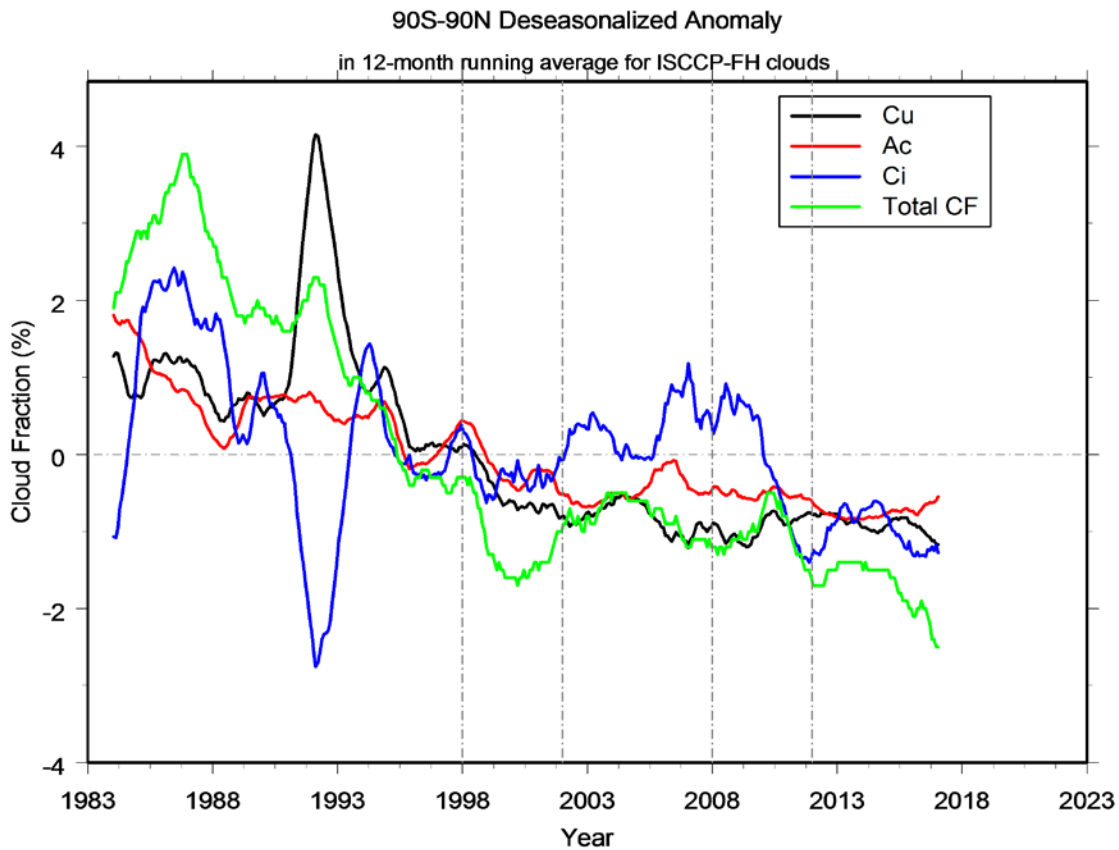
525

526

527

528

529



530

531 **Figure 4.** Deseasonalized anomalies (shown as 12-month running averages) of global monthly
 532 mean total (green curve) cloud amount (%) and the amounts of cirrus (blue curve), altocumulus
 533 (red curve) and cumulus (black curve) as defined by in ISCCP-H but modified for FH: added
 534 cumulus to account for upper-level-cloud overlap and shifted altocumulus to cirrus to account for
 535 effect of cloud overlap with cirrus.

536

537 Ever since the late 1980s, the ISCCP cloud dataset has shown an overall decline of global
 538 mean cloud amount (CA), now also seen in other datasets (Karlsson and Devasthale 2018). The
 539 decrease in ISCCP CA is about 0.06 from 1986-2018, which may be exaggerated by 0.01-0.02 by
 540 artifacts in earlier years (Rossow et al., 2022). The large variations in the early 1990s are caused
 541 by identification as cloud of some of the thick stratospheric aerosol from the Mt. Pinatubo volca-
 542 no. Looking at the variations of cloud types, defined in ISCCP by combinations of cloud top
 543 pressure-optical thickness and phase, shows that the global decrease appears solely in the optical-
 544 ly thinnest types, mostly cumulus (Cu) and altocumulus (Ac) with some cirrus (Ci), as shown in
 545 Fig. 4 (as other cloud types show no changes, they are not shown). The results shown here are
 546 the version used in FH, where there have been adjustments of the ISCCP-H cloud type amounts
 547 that add some Cu amount and shift some middle-level clouds to cirrus to account for layer-
 548 overlap effects (cf. Rossow and Zhang 2010), increasing/decreasing the magnitude of the Ci/Ac

549 changes. As there is no corresponding increase in the optically thicker cloud types, this change is
 550 not consistent with a drift of the VIS calibration (cf. Rossow and Ferrier, 2015), even though the
 551 overall average optical thickness does increase because of the decreased amount of thinner
 552 clouds included in the average. Moreover, if a drift of VIS calibration were the cause, the chang-
 553 es in these three cloud types would be strongly correlated, but only the changes in Cu and Ac are
 554 correlated (coefficient $r \approx 0.8$), not Ci ($r < 0.4$ with Ac but $r \approx 0$ with Cu). The key is that total
 555 CA in the ISCCP data is insensitive to calibration changes (see Fig. 2.2 in Appendix 2 in
 556 Stubenrauch et al. 2012) because the cloud detection each month is made relative to that month's
 557 determination of clear radiances: the global mean surface reflectance shows no trend. There is
 558 also supporting evidence from CERES, as shown in Fig. 2, indicating a decline in the global
 559 mean albedo since the early 2000s (Loeb et al., 2021), and from an observed corresponding in-
 560 crease in surface solar insolation in the 1990s (Wild et al., 2005; Pinker et al., 2005).

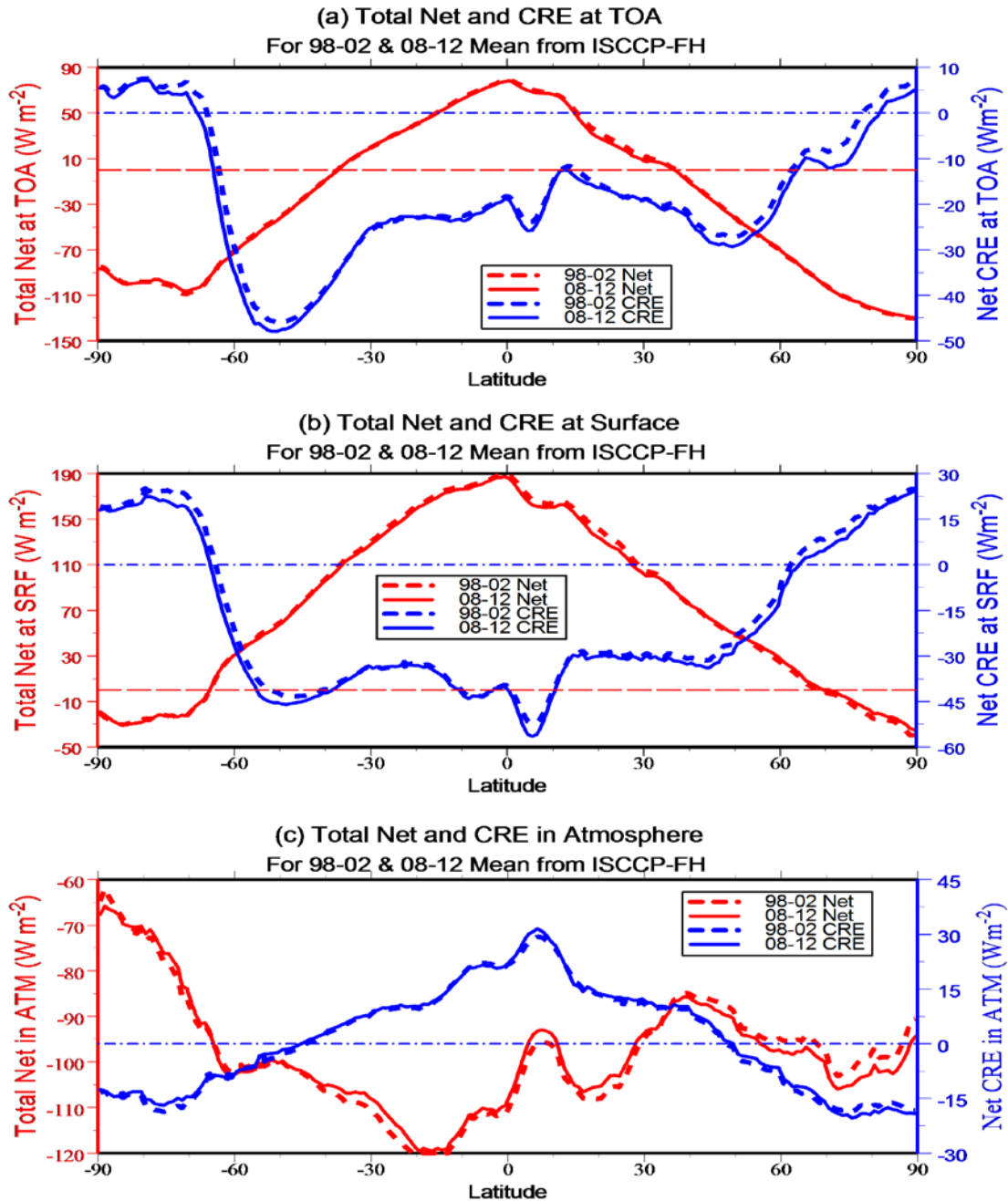
561 Although the simultaneous variations of many cloud, atmosphere and surface properties
 562 effect the flux anomalies (Fig. 2, 3), the leading single-variable anomaly correlations (calculated
 563 for month-to-month variations over global maps at 110 km scale) are as follows (all other corre-
 564 lation values are much smaller). At TOA, the leading correlation with variations of SWnet is
 565 changes of Cu amount ($r \approx -0.5$), which are, in turn, correlated with T_S variations ($r \approx 0.7$, but
 566 this connection might be distorted by the fact that the T_S values come from satellite infrared
 567 measurements, which are clear-sky biased). The variations of SWcre are dominated by overall
 568 changes in optical thickness ($r \approx -0.8$). The TOA LWnet variations are strongly correlated with
 569 changes in Ac amount ($r \approx 0.7$) and secondarily with changes in mid-troposphere water vapor (r
 570 ≈ 0.5); however, the changes in TOA LWcre are dominated by changes in Ci amount ($r \approx 0.8$)
 571 and near-surface air temperature, T_a ($r \approx 0.7$), but not the mid-troposphere temperature (T_{500} $r <$
 572 0.2). Correlations of SRF SWnet are similar to those at TOA, but the SRF LWnet and LWcre are
 573 more correlated with temperature and humidity changes than with cloud changes (although Ci
 574 amount variations explain some of the LWcre variance). The ATM SWnet is much more strongly
 575 affected by atmospheric humidity changes (precipitable water at mid-troposphere, PW500 $r \approx$
 576 0.8), but the SWcre changes are dominated by changes in Ci amount ($r \approx -0.8$). Likewise the
 577 ATM LWnet and LWcre are affected most by changes in atmospheric temperature ($r \approx -0.5$, 0.7
 578 respectively, with T_a), although Ci amount is equally important to LWcre variations ($r \approx 0.8$).

579

580 **6 Discussion of some possible feedbacks implied in an example of transient change**

581 The period from the late 1990s to the early 2010s is notable for a number of reasons: (1)
 582 it was framed at the beginning by a very strong El Nino in 1997-1998 and La Nina from 1999-
 583 2001 and at the end by a strong La Nina in 2010-2012 with some weaker events in between
 584 (www.cpc.ncep.noaa.gov/data/indices/oni.ascii.txt), (2) the PDO index tracked the ENSO index
 585 in these framing events from strongly positive switching to negative at the beginning to persis-
 586 tently negative at the end, but weakly positive in between
 587 (www.ncei.noaa.gov/pub/data/cmb/ersst/v5/index/ersst.v5.pdo.dat), and (3) there was a signifi-
 588 cant slowing of the rate of increase of global annual mean surface temperature as compared to
 589 the decades before and after this period (www.data.giss.nasa.gov/gistemp, see also Loeb et al.,
 590 2021). Figure 2 shows that the period from 1998 to 2012 was characterized in the FH data by a
 591 steady decrease of TOA SWnet (less heating) by a little more than 1.5 Wm^{-2} and an increase of

592 TOA LWnet (less cooling) by a little more than 0.5 Wm^{-2} , giving an overall decrease TOA net
 593 flux by a little less than 1 Wm^{-2} (all quoted values are based on averages over 1998-2002 and
 594 2008-2012 to represent the trends, Table 4). Figure 3 shows a very similar anomaly of SRF
 595 SWnet with no significant change of SRF LWnet in the period. Figure 4 shows a general increase
 596 of cirrus cloud amount by almost 0.02 over this period (with a much smaller decrease of cumu-
 597 lus) and altocumulus, resulting in a near-constant total cloud amount during this period.



598
 599

600 **Figure 5.** Zonal mean Total Net Flux (red curves) and Cloud Radiative Effect (CRE, blue
 601 curves) in Wm^{-2} versus latitude averaged over two 5-yr periods (dashed curves 1998-2002, solid

602 curves 2008-2012): (a) at TOA, (b) at surface and (c) in atmosphere. These two periods corre-
 603 spond, respectively, with positive and negative anomalies in TOA SWnet and negative and posi-
 604 tive anomalies in TOA LWnet (Fig. 2). See Table 4.

605
 606

607 Figure 5a shows the zonal mean distribution of total net radiation and cloud radiative ef-
 608 fect (CRE) at TOA averaged over the two time periods (1998-2002, 2008-2012) that correspond
 609 (Fig. 2), respectively, to the positive and negative anomalies of TOA SWnet and the negative and
 610 positive anomalies of TOA LWnet. The familiar total net flux distribution at TOA shows a net
 611 heating ($|\text{SWnet}| > |\text{LWnet}|$) in low to middle latitudes and a net cooling ($|\text{SWnet}| < |\text{LWnet}|$) at
 612 higher latitudes (cf. Zhang and Rossow, 1997; see also Kato et al., 2008). The net effect of clouds
 613 is to decrease lower latitude heating and increase higher latitude cooling (both negative CRE),
 614 except right at the poles where CRE is positive (cf. Zhang et al., 2004). The small SW and LW
 615 changes between these two periods (see Table 4) are accounted for by cloud changes; although
 616 other atmospheric and surface properties play a role in the LW changes as discussed above (cf.
 617 Loeb et al. 2021), they are specifically related to the increase of cirrus in this particular period.

618

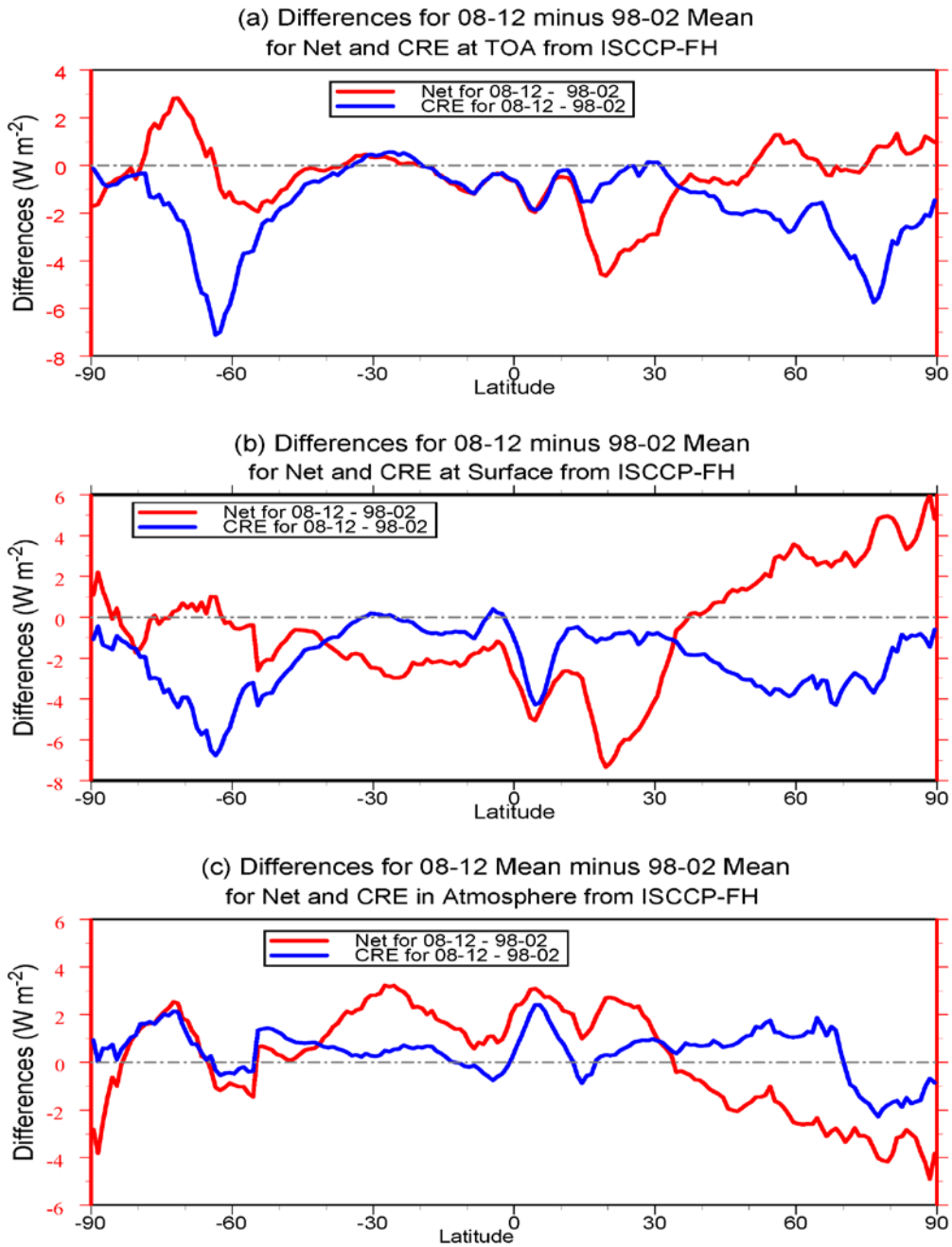
619 **Table 4.** Mean Net Fluxes and Cloud Radiative Effects at TOA, at Surface and in Atmosphere
 620 for 1998 to 2002 and 2008 to 2012 periods in Wm^{-2} .

	SWnet	LWnet	Net	SWcre	LWcre	NETcre
TOA						
1998-2002 mean	237.1	-232.8	4.3	-48.0	26.3	-21.7
2008-2012 mean	235.5	-232.0	3.5	-49.8	26.8	-22.9
Surface						
1998-2002 mean	160.3	-53.4	107.0	-50.6	21.6	-29.0
2008-2012 mean	158.8	-53.5	105.3	-52.4	21.6	-30.8
Atmosphere						
1998-2002 mean	76.8	-179.4	-102.6	2.6	4.7	7.3
2008-2012 mean	76.8	-178.5	-101.8	2.7	5.2	7.9

621

622 The global near-balance of TOA radiation splits into predominately SW heating of the
 623 surface and LW cooling of the atmosphere with clouds effects decreasing both as shown in Fig.
 624 5b and 5c and Tables 3 and 4 (cf. Zhang et al., 2004). The surface radiative heating (Fig. 5b) de-
 625 creases with latitude becoming net cooling in the annual mean only in the polar regions because
 626 of lack of solar heating in winter. The LW cooling at the polar surface is about $20\text{-}30 \text{ Wm}^{-2}$
 627 stronger in FH, the only significant change from FD. The new results are much closer to surface
 628 measurements in the north (Persson et al., 2002), but are too strong by $10\text{-}20 \text{ Wm}^{-2}$ in winter in
 629 the south (Van Den Broeke et al., 2005). The cloud effects at SRF decrease this heating at most
 630 latitudes (negative CRE) but cause surface heating at the poles (positive CRE). In other words
 631 clouds act to reduce the meridional gradient of surface heating that forces (in part) the oceanic
 632 circulation (cf. Zhang and Rossow, 1997; Kato et al., 2008, Matus and L'Ecuyer, 2017). The net

633 atmospheric cooling (Fig. 5c) is much larger at low to middle latitudes than in the polar regions
 634 (the polar cooling is much stronger in the north than in the south), overall following atmospheric
 635 temperature (more cooling at higher temperature). Clouds reduce the ATM cooling at low to
 636 middle latitudes (positive CRE) and enhance it in the polar regions (negative CRE). In other
 637 words clouds act to reduce the meridional gradient of atmospheric cooling, effectively enhancing
 638 the heating gradient that forces the atmospheric circulation (cf. Zhang and Rossow, 1997; Kato et
 639 al., 2008, Matus and L'Ecuyer. 2017).



642 **Figure 6.** Differences between two 5-yr periods (2008-2012 minus 1998-2002) of the zonal
 643 mean Total Net Flux (red curve) and ATM CRE (blue curve) in Wm^{-2} versus latitude: (a) at
 644 TOA, (b) at surface and (c) in atmosphere.

645

646 All of the decrease of TOA SWnet (less heating) between 1998 and 2012 occurred at SRF
 647 and all of the increase of TOA LWnet (less cooling) occurred in the atmosphere (Table 4). The
 648 corresponding very small changes in the latitudinal distribution of net fluxes and CRE in Fig. 5
 649 are better shown in Fig. 6 as the differences, 2008-2012 average minus 1998-2002 average, rep-
 650 resenting the trend from 1998 to 2012. The global average decrease of TOA total net flux over
 651 this period appears as a decrease at low to middle latitudes, but there is also an increase (reduced
 652 cooling) in the polar regions (Fig. 6a). The global mean decrease of total net flux at TOA is
 653 caused almost entirely by cloud effects on the SW offset by a weak effects on LW: Fig. 6a shows
 654 that the CRE difference is (mostly) negative at all latitudes but much more so at higher latitudes.
 655 However the changes in TOA total net flux conflate changes in SW forcing at the surface with
 656 changes in the LW response of the atmosphere, so separating the TOA changes into their SRF
 657 and ATM components better reveals what happened between 1998 and 2012. To keep the signs
 658 straight in what follows, the surface net flux changes are described as increases/decreases of
 659 heating and the atmospheric net flux changes are described as increases/decreases of cooling.

660 The net flux changes at SRF from 1998-2002 to 2012-2016 (Fig. 6b) show a very differ-
 661 ent pattern in the two hemispheres. The heating in the tropics decreased (negative difference),
 662 more strongly in the north than the south; the cooling at the poles also decreased (positive differ-
 663 ence), again more strongly in the north than the south. These differences represent a decrease in
 664 the equator-to-pole heating gradient over this period. At middle latitudes the surface heating de-
 665 creased in the southern hemisphere and increased in the northern hemisphere, but this pattern
 666 seems consistent with the overall change of the PDO index from positive to negative over this
 667 period, which would be a negative change of SST in the tropical Pacific and positive change of
 668 SST in the north Pacific. The overall pattern of change implies a weaker meridional gradient in
 669 radiative heating forcing of the oceanic circulation, consistent with the cooling (warming) of SST
 670 in the tropics (midlatitudes). These net flux changes are opposed by the cloud changes: negative
 671 SRF CRE at lower latitudes shows only a very small decrease (becoming more negative) in the
 672 tropics and subtropics, but more substantial decreases at higher midlatitudes, related to the small
 673 decrease of cumulus and altocumulus clouds. Near the poles, where the SRF Net switches from
 674 negative to positive, it also decreases (becoming less positive). The CRE on surface heating is
 675 caused by decreased cumulus and altocumulus amounts. If the cloud-induced radiative flux
 676 changes from 1998 to 2012 – a smaller cloud-induced decrease of the meridional heating gradi-
 677 ent (that is, tending to make the heating gradient larger) – are indirectly related (through ocean-
 678 atmosphere interaction) to a change of the ocean circulation associated with the reduced meridi-
 679 onal temperature gradient (positive to negative PDO index), then they imply a positive cloud-
 680 radiative feedback on the ocean circulation.

681 From 1998-2002 to 2008-2012, the ATM cooling decreased at lower latitudes (positive
 682 difference, a heating) and increased at higher latitudes (negative difference, a cooling), especially
 683 in the northern hemisphere (Fig. 6c). This implies an enhancement of the meridional radiative
 684 cooling gradient forcing the atmospheric circulation. The positive ATM CRE at low latitudes

685 slightly increased (more heating related to increased cirrus) and the negative ATM CRE in the
686 polar regions behaved differently in the north and south, decreasing in the north (decreased cool-
687 ing effect) and increasing in the south (increased cooling effect). If these cloud-radiative changes
688 are caused by a weakening of the atmospheric circulation, as might be expected from the de-
689 crease of the SST meridional gradient with the PDO phase change (see Chen et al., 2002 that find
690 a strengthening circulation for an opposite trend in the 1990s), then the cloud changes imply a
691 negative feedback on the atmospheric circulation.

692 The opposite sense of these (possible) transient cloud-radiative feedbacks on the coupled
693 atmospheric and oceanic circulations on a decadal time scale comes about because of the sepa-
694 rate SW heating of SRF and LW cooling of ATM and because of the different SW and LW CRE
695 by different cloud types. A similar opposite effect is seen in the partitioning of average cloud-
696 radiative effects on the mean circulations discussed in Zhang and Rossow (1997) and Kato et al.
697 (2008).

698

699 **7 Conclusions**

700 There are now three global data products that provide calculated, cloud-modified, atmos-
701 pheric radiative heating rate profiles: one based on CloudSat/CALIPSO (2B-FLXHR, L'Ecuyer
702 et al., 2008, also L'Ecuyer et al., 2019 and Hang et al., 2019), one based on CERES (latest ver-
703 sion, Ed4.0, described in Loeb et al. 2018) and one based on ISCCP-H, called FH reported here
704 (see also Zhang 2017), a revised version of ISCCP-FD (Zhang et al., 2004). The calculated flux
705 profiles in the first product are based on direct radar-lidar measurements from satellites of cloud
706 layer location and thickness, as well as estimates of cloud water content, with very high vertical
707 resolution, covering four years at twice-daily sampling, but with very sparse spatial sampling
708 (e.g., L'Ecuyer et al., 2008, show that their calculated TOA fluxes exhibit the best agreement
709 with CERES results when averaged to spatial intervals of 5° and over a whole year). The com-
710 bined radar-lidar measurements still slightly underestimate the amount of very low-level cloudi-
711 ness because of ground-clutter effects on the radar measurements (L'Ecuyer et al., 2008) and be-
712 cause some low cloudiness is hidden below thicker upper-level clouds that the lidar cannot pene-
713 trate (Henderson et al., 2013, evaluate the effects of the estimated missed cloud amounts). The
714 calculated flux profiles in the CERES products cover a longer time period (currently about 20 yr)
715 and are constrained by direct, four-times-daily TOA flux measurements. These flux profiles em-
716 ploy additional satellite cloud products and reanalysis model atmospheric properties to interpo-
717 late the direct measurements to 1-hr time intervals, effectively assuming single-layer clouds in
718 each scene with no detail below the 500 hPa level (Rose et al., 2013). While the TOA SW flux is
719 a strong constraint on the calculated CERES profiles of SW, the TOA LW flux is a much weaker
720 constraint. Haynes et al. (2013) contrast the high vertical resolution of the 2B-FLXHR heating
721 rate profile with the very low vertical resolution CERES product in their Fig. 1.

722

723 The horizontal lines in Fig. 1 indicate the vertical intervals in the FH (and FD) profiles,
724 both of which augment the ISCCP cloud type information with a statistical CVL model account-
725 ing for cloud layer overlap (revised for FH based on RL-GEOPROF). Although still crude in the
726 vertical compared to 2B-FLXHR profiles but with much better space-time sampling, the FH (and
727 FD) profiles still capture the basic low-middle-high features of the cloud distribution in the fig-
728 ure. Based on the sensitivity studies of the effects of changing cloud vertical layers on the flux

729 profiles, discussed in Section 4, the long-term changes in three cloud types shown in Fig. 4 imply
730 the following: the decrease of cumulus and altocumulus decreases LWnet in the lower atmos-
731 phere and surface by $< 3 \text{ Wm}^{-2}$ reinforced by a smaller decrease of cirrus that also causes a simi-
732 lar magnitude net flux decrease in the upper atmosphere. The SW flux profile is insensitive to
733 such small changes. Overall, the long-term change in clouds do not appear to have changed the
734 radiative flux profile shapes in the global mean, but regional changes may be more significant.
735 However, decrease of low cloud amount shows up as a decrease of SRF LWdn in Fig. 3a. Look-
736 ing at the longer FH record, the overall decrease in cumulus and altocumulus amounts appears to
737 be offset by a small increase in cloud optical thickness (see Fig. 5 in Rossow et al., 2022) such
738 that SWnet heating at TOA and SRF increased slightly and the LWnet cooling at TOA/ATM
739 (SRF) increased (decreased) (Fig. 2 and 3). However, these changes, if accurate, are all < 2
740 Wm^{-2} .

741

742 As discussed here, the overall estimated uncertainty of monthly average regional (110 km
743 scale) FH fluxes increases from $< 10 \text{ W/m}^2$ at TOA up to $< 15 \text{ W/m}^2$ at the surface; the uncer-
744 tainties at intermediate levels are in between these two. Although differences between FH fluxes
745 and the matched direct measurements at 110 km and 3 hr scales are larger, the scatter with the
746 comparison measurements appears to be caused more by mismatched spatial scales, meteorolog-
747 ical conditions, and observation times (cf. Rossow and Zhang, 1995, Zhang et al., 2004, 2010 for
748 more detailed evaluations). Typical magnitudes of flux variation at this smaller scale are general-
749 ly larger (10's of Wm^{-2}) than the estimated uncertainties, produced mostly by cloud variations,
750 which are larger in time than space because the cloud amount distribution is "U-shaped" (cf.
751 Rossow et al., 1993, Rossow and Cairns, 1995) with cloud amount < 0.1 occurring more than
752 15% and > 0.9 more than 40% of the time. There are some surface regimes (LW in polar and
753 tropical areas) where the FH space-time flux variations are smaller than the estimated uncertain-
754 ties, which suggests that our estimates of random uncertainty are conservative. The main limita-
755 tion of FH accuracy in the SW is related to variations of the cloud microphysical properties
756 (which are fixed in the calculations), especially for ice clouds. In LW, especially at the surface,
757 the main limitation is related to the uncertainty in the ancillary atmospheric temperature-
758 humidity data.

759 The accuracy of the FH fluxes is still sufficient, compared with the magnitude of local
760 (110 km), 3-hourly variations, for diagnosing weather-to-seasonal scale variations of radiation
761 induced by changes in cloudiness as well as atmospheric and surface properties. Together with
762 the variety of other satellite measurements, especially multi-spectral imagers, infrared spec-
763 trometers, microwave temperature-humidity sounders and active cloud and precipitation profil-
764 ers, these results can be combined with global reanalyses of atmospheric motions to diagnose
765 energy and water exchanges in the whole range of weather systems, e.g., analyses such as Jakob
766 and Schumacher (2008), Haynes et al. (2011), Oreopolus and Rossow (2011), Booth et al.
767 (2013), Polly and Rossow (2016), Masunaga and Luo (2016), Rossow et al. (2016), and those
768 associated with slower "climate" variations such as MJO, seasons, and ENSO events, e.g., anal-
769 yses such as Zhang and Rossow (1997), Kato et al. (2008), Tromeur and Rossow (2010). The
770 clouds and radiative flux effects in weather and climate models can be evaluated, e.g., Tselioudis
771 et al. (2021).

772

773 On the larger scale of interannual variations of the atmospheric and oceanic general circu-
774 lations, these newer radiative flux products can be combined with newer global datasets quanti-

775 fying precipitation, water vapor, surface turbulent fluxes, ocean surface and atmospheric winds,
776 and temperatures to calculate the mean energy and water transports (updating Zhang and Rossow
777 1997, Kato et al., 2008 for example, see also Stephens et al., 2016). The general energetics of the
778 atmospheric circulation can also be determined (updating Romanski and Rossow, 2013 for ex-
779 ample). An example of such a data collection is the 15-yr GEWEX Integrated Data Product
780 (Kummerow et al., 2019). Direct quantitative diagnosis of the transient feedbacks on these circu-
781 lations and exchanges by cloud processes is now possible. The advantage of using ISCCP-FH for
782 such studies, in addition to the higher time resolution and longer record than other products, is
783 that the causes of variations in radiative heating of the atmosphere and surface can be made di-
784 rectly, separating cloud effects from other causes at weather-to-interannual scales.

785 786 **Acknowledgments**

787 We would like to give special thanks to Dr. Reto Reudy who helped separate the radia-
788 tion code (RadE) from NASA GISS GCM ModelE that makes possible to initiate the ISCCP-FH
789 project. We also especially thank Dr. Andrew A. Lacis and Dr. Valdar Oinas who participated in
790 the development of the radiation code for the ISCCP-FH project that made possible the ISCCP-
791 FH flux data production. The development of the ISCCP-FH production code was funded by
792 NOAA Climate Data Record Project (Grant NA11NES4400002 for 2011–2014). Computer facil-
793 ities are supplied by NOAA's National Centers for Environmental Information and NASA God-
794 dard Institute for space Studies. We thank Dr. Stefan Kinne who has provided us with AeroCom,
795 MACv1 and MACv2, aerosol datasets. We also thank Dr. Paul W. Stackhouse and Dr. Shashi K.
796 Gupta who have provided us with TSI datasets. Finally we thank CERES and BSRN teams for
797 providing us with their datasets for the evaluation of the ISCCP-FH products.

798

799 **Open Research**

800 ISCCP-FH flux profile data products and documents can be accessed and downloaded through login
801 at <https://isccp.giss.nasa.gov/projects/flux.html>. CERES SYN1deg Ed4 data may be ordered from
802 <https://ceres.larc.nasa.gov/data/#syn1deg-level-3>, and for data Quality Summary, see
803 https://ceres.larc.nasa.gov/documents/DQ_summaries/CERES_SYN1deg_Ed4A_DQS.pdf. (Regis-
804 tration is required). BSRN data can be obtained from

805 <https://bsrn.awi.de/other/publications/establishment-and-development-of-the-bsrn/>. (Registration is
806 required).

807

808

809 **References**

810

811 Barkstrom, B., Harrison, E., Smith, G., Green, R., Kibler, J., Cess, R., & the ERBE Science
812 Team (1989). Earth Radiation Budget Experiment (ERBE) archival and April 1985 results. *Bull.*
813 *Amer. Meteor. Soc.*, 70 (10), 1254-1262, doi:10.1175/1520-
814 0477(1989)070<1254:erbeaa>2.0.co;2.

815

816 Booth, J.F., Naud, C.M., & Del Genio, A.D. (2013). Diagnosing warm frontal cloud formation
817 in a GCM: A novel approach using conditional subsetting. *J. Climate*, 26, 5827-5845,
818 doi:10.1175/jcli-d-12-00637.1.

819

820 CERES Science Team (2013). CERES_SYN1deg_Ed3A Data Quality Summary, at
821 https://ceres.larc.nasa.gov/documents/DQ_summaries/CERES_SYN1deg_Ed3A_DQS.pdf.

822

823 Chen, J., Carlson, B.E., & Del Genio, A.D. (2002). Evidence for the strengthening of the tropical
824 general circulation in 1990s. *Science*, 295, 838-841, doi:10.1126/science.1065835.

825

826 Chen, T., Zhang, Y-C. & Rossow, W.B. (2000). Sensitivity of atmospheric radiative heating rate
827 profiles to variations of cloud layer overlap. *J. Climate*, 13, 2941-2959, doi:10.1175/1520-

828 0442(2000)013<0264:reoctv>2.0.co;2.

829

830 Chen, T., & Rossow, W.B. (2002). Determination of top-of-atmosphere longwave radiative flux-
831 es: A comparison between two approaches using ScaRab data. *J. Geophys. Res.*, 107, D8, (1-14),
832 doi:10.1029/2001jd000914.

833

834 DeAngelis, A.M., Qu, X., Zelinka, M.D., & Hall, A. (2015). An observational radiative con-
835 straint on hydrologic cycle intensification, *Nature*, 528, 249-253, doi:10.1038/nature15770.

836

837 Driemel, A., Augustine, J., Behrens, K., Colle, S., Cox, C., Cuevas-Agulló, E., Denn, F., et al.
838 (2018). Baseline Surface Radiation Network (BSRN): structure and data description (1992–
839 2017), *Earth Syst. Sci. Data*, 10, 1491–1501, <https://doi.org/10.5194/essd-10-1491-2018>, 2018.

840

841 GISTEMP Team (2021). GISS Surface Temperature Analysis (GISTEMP), version 4. NASA
842 Goddard Institute for Space Studies. Dataset accessed 20YY-MM-DD at
843 <https://data.giss.nasa.gov/gistemp/>.

844

845

846 Goode, P.R., Palle, E., Shoumko, A., Shoumko, S., Montanes-Rodriguez, P., & Koonin, S.E.
847 (2021). Earth's albedo 1998-2017 as measured from earthshine. *Geophys. Res. Lett.*, 48, (1-8),
848 doi:10.1029/2021gl094888.

849

850 Hang, Y., L'Ecuyer, T.S., Henderson, D., Matus, A.V. & Wang, Z. (2019). Reassessing the role
851 of cloud type in Earth's radiation budget after a decade of active spaceborne observations. Part
852 II: Atmospheric heating, *J. Climate*, 32, 6219-6236, doi:10.1175/jcli-d-18-0754.1.

853
854 Hansen, J., Fung, I., Lacis, A., Rind, D., Lebedeff, S., Ruedy, R., et al. (1988). Global climate
855 changes as forecast by the Goddard Institute for Space Studies three-dimension model, *J Ge-*
856 *ophys. Res.*, 93, 9341-9364, 1988.

857
858 Haynes, J.M., Jakob, C., Rossow, W.B., Tselioudis, G., & Brown, J. (2011). Major characteris-
859 tics of southern ocean cloud regimes and their effects on the energy budget. *J. Climate*, 24, 5061-
860 5080, doi:10.1175/2011jcli4052.1.

861
862 Haynes, J. M., Vonder Haar, T.H., L'Ecuyer, T., & Henderson, D. (2013). Radiative heating
863 characteristics of Earth's cloudy atmosphere from vertically resolved active sensors, *Geophys.*
864 *Res. Letters*, 40, doi:10.1002/grl.50145.

865
866
867
868 Jacob, C., & Schumacher, C. (2008). Precipitation and latent heating characteristics of the major
869 tropical western Pacific cloud regimes. *J. Climate*, 21, 4348-4364. doi:10.1175/2008jcli2122.1.

870
871 Jin, Y., & Rossow, W.B. (1997). Detection of cirrus overlapping low-level clouds. *J. Geophys.*
872 *Res.*, 102, 1727-1737, doi:10.1029/96jd02996.

873

874 Karlsson, K-G., & Devasthale, A. (2018). Inter-comparison and evaluation of the four longest
875 satellite-derived cloud climate data records: CLARA-A2, ESA Cloud CCI V3, ISCCP-HGM and
876 PATMOS-x. *Remote Sensing*, 2018, 10, 1567, (1-27), doi:10.3390/rs10101567.

877

878 Kato, S., Rose, F.G., Rutan, D.A., & Charlock, T.P. (2008). Cloud effects on the meridional at-
879 mospheric energy budget estimated from Clouds and the Earth's Radiant Energy (CERES) data.
880 *J. Climate*, 21, 4223-4241, doi:10.1175/2008jcli1982.1.

881

882 Kelley, M., Schmidt, G.A., Nazarenko, L.S., Bauer, S.E., Ruedy, R., Russell, G. L., et al. (2020).
883 GISS-E2.1: Configurations and climatology. *J. Adv. Modeling Earth Sys*, 12, e2019MS002025.
884 Doi: 10.1029/2019MS002025.

885

886 Kinne, S., O'Donnel, D., Stier, P., Kloster, S., Zhang, K., Schmidt, H., et al. (2013). MAC-v1: A
887 new aerosol climatology for climate studies. *J. Adv. Modeling Earth Sys.*, 5, 704-740,
888 doi:10.1002/jame.20035.2013.

889

890 Kinne, S. (2019). The MACv2 aerosol climatology. *Tellus B: Chem. Phys. Meteor.*, 71(1), 1–21.
891 <https://doi.org/10.1080/16000889.2019.1623639>.

892

893 Kohsiek, W., Liebenthal, C., Foken, T., Vogt, R., Oncley, S.P., Bernhofer, Ch., & Debruin,
894 H.A.R. (2006). The Energy Balance Experiment EBEX-2000. Part III: Behavior and quality of
895 the radiation measurements. *Boundary-Layer Meteor.*, (1-21), doi:10.1007/s10546-006-9135-8.

896

897 Kummerow, C., Brown, P., Adler, R., Kinne, S., Rossow, W., Stackhouse, P. et al. (2019). The
898 GDAP integrated product. *GEWEX NEWS*, 29, 3-6.

899
900 Lacis, A. A., & Oinas, V. (1991). A description of the correlated k distributed method for model-
901 ing nongray gaseous absorption, thermal emission, and multiple scattering in vertically inhomo-
902 geneous atmospheres. *J. Geophys. Res.*, 96, 9027-9063, doi:10.1029/90jd01945.

903

904 L'Ecuyer, T. S., Wood, N., Haladay, T., & Stephens, G.L. (2008). The impact of clouds on at-
905 mospheric heating based on the R04 CloudSat fluxes and heating rate dataset, *J. Geophys. Res.*,
906 113, doi: 10.1029/2008JD009951.

907

908 L'Ecuyer, T.S., Hang, Y., Matus, A.V., & Wang, Z. (2019). Reassessing the role of cloud type
909 in Earth's radiation budget after a decade of active spaceborne observations. Part I: Top of at-
910 mosphere and surface, *J. Climate*, 32, 6197-6217, doi:10.1175/jcli-d-18-0753.1.

911

912 Liao, X., Rossow, W.B., & Rind, D. (1995). Comparison between SAGE II and ISCCP high-
913 level clouds, Part II: Locating cloud tops. *J. Geophys. Res.*, 100, D1, 1137-1147,
914 doi:10.1029/94jd02430.

915

916 Liu, Z., Kar, J., Zeng, S., Tackett, J., Vaughan, M., Avery, M., et al., (2019). Discriminating be-
917 tween clouds and aerosols in the CALIOP version 4.1 data products. *Atmos. Meas. Tech.*, 12,
918 703-734, doi:10.5194/amt-12-703-2019.

919

920 Loeb, N.G., Priestley, K. J., Kratz, D. P., Geier, E. B., Green, R. N., Wielicki, B. A., et al.
921 (2001). Determination of unfiltered radiances from the Clouds and the Earth's Radiant Energy
922 System instrument. *J. Appl. Meteor.*, 40, 822-835, doi:10.1175/1520-
923 0450(2001)040<0822:dourft>2.0.co;2.

924

925 Loeb, N.G., Wielicki, B.A., Doelling, D.A., Smith, G.L., Keyes, D.F., Kato, S., et al. (2009).
926 Toward optimal closure of Earth's top-of-atmosphere radiation budget. *J. Climate*, 22, 748-766,
927 doi:10.1175/2008jcli2637.1.

928

929 Loeb, N.G., Doelling, D.R., Wang, H., Su, W., Nguyen, C., Corbett, J. G., et al. (2018). Clouds
930 and the Earth's Radiant Energy System (CERES) Energy Balanced and Filled (EBAF) top-of-
931 atmosphere (TOA) Edition-4.0 data product. *J. Climate*, 31, 894-918, doi:10.1175/jcli-d-17-
932 0208.1.

933

934 Loeb, N.G., Johnson, G.C., Thorsen, T.J., Lyman, J.M., Rose, F.G., & Kato, S. (2021). Satellite
935 and ocean data reveal marked increase in Earth's heating rate. *Geophys. Res. Lett.*, 48, (1-8),
936 doi:10.1029/2021gl093047.

937

938 Mace, G.G., & Zhang, Q. (2014). The CloudSat radar-lidar geometric profile product (RL-
939 GeoProf): Updates, improvements, and selected results. *J. Geophys. Res. Atmos.*, 119, 9441-
940 9462, doi:10.1002/2013jd021374.

941

942 Masunaga, H., & Luo, Z. J. (2016). Convective and large-scale mass flux profiles over tropical
943 oceans determined from synergistic analysis of a suite of satellite observations. *J. Geophys. Res.*
944 *Atmos.*, 121, 7958-7974, doi:10.1002/2016jd024753.

945

946 Matus, A.V., & L'Ecuyer, T. (2017). The role of cloud phase in Earth's radiation budget. *J. Ge-*
947 *ophys. Res. Atmos.*, 122, 2559-2578, doi:10.1002/2016jd025951.

948

949 Michalsky, H., Dutton, E., Rubes, M., Nelson, D. Stoffel, T., Wesley, M., et al., (1999). Optimal
950 measurement of surface shortwave irradiance using current instrumentation. *J. Atmos. Ocean*
951 *Tech.*, 16, 55-69, doi:10.1175/1520-0426(1999)016<0055:omossi>2.0.c0;2.

952

953 Ohmura, A., Dutton, E.G., Forgan, B., Frohlich, C. Gilgen, H., Hegner, H., et al. (1998). Base-
954 line Surface Radiation Network (BSRN/WCRP): New precision radiometry for climate research.
955 *Bull. Amer. Meteor. Soc.*, 79 (10), 2115-2136, doi:10.1175/1520-
956 0477(1998)079<2115:bsrnbw>2.0.co;2.

957

958 Oreopoulos, L., & Rossow, W. B. (2011). The cloud radiative effect of ISCCP weather states. *J.*
959 *Geophys. Res.*, 116, (1-22), doi:10/1029/2010jd015472.

960

961 Oreopoulos, L., Mlawer, E., Delamere, J., Shippert, T., Cole, J., Fomin, B., et al. (2012). The
962 Continual Intercomparison of Radiation Codes: Results from Phase I. *J. Geophys. Res.*, 117,
963 D06118, (1-19), doi:10.1029/2011jd016821.

964

965 Persson, P.O.G., Fairall, C.W., Andreas, E.L., Guest, P.S., & Perovich, D.K. (2002). Measure-
966 ments near the atmospheric surface flux group tower at SHEBA: Near-surface conditions and
967 surface energy budget. *J. Geophys. Res.*, 107, 8045, (1-21), doi:10.1029/2000jc000705.

968
969 Philipona, R., Dutton, E.G., Stoffel, T., Michalsky, J., Reda, I., Stifter, A., et al. (2001). Atmos-
970 pheric longwave radiance uncertainty: Pyrgeometers compared to an absolute sky-scanning radi-
971 ometer, atmospheric emitted radiance interferometer, and radiative transfer model calculations. *J.*
972 *Geophys. Res.*, 106, D22, 28,129-28,141, doi:10.1029/200jd000196.

973
974 Pinker, R.T., Zhang, B., & Dutton, E.G. (2005). Do satellites detect trends in surface solar radia-
975 tion? *Science*, 308, 850-854, doi:10.1126/science.1103159.

976
977 Polly, J., & Rossow, W.B. (2016). Distribution of midlatitude cyclone attributes based on the
978 MCMS database. *J. Climate*, 6483-6507, doi:10.1175/jcli-d-15-0857.1.

979
980 Protat, A., Young, S.A., McFarlane, S.A., L'Ecuyer, T., Mace, G.G., Comstock, J.M. et al.
981 (2014). Reconciling ground-based and space-based estimates of the frequency of occurrence and
982 radiative effect of clouds around Darwin, Australia, *J. Appl. Meteor. Climatol.*, 53, 456-478,
983 doi:10.1175/jamc-d-13-072.1.

984
985 Raschke, E., Kinne, S., & Stackhouse, P.W. (2012). GEWEX Radiation Flux Assessment (RFA),
986 WCRP Report 19/2012, Vol. 1: Scientific Results, Vol. 2: Appendices and details [available at
987 <http://www.wcrp-climate.org/documents/GEWEX%20RFA-Volume%201-report.pdf>]

988

989 Raschke, E., Kinne, S., Rossow, W.B., Stackhouse, P.W., & Wild, M. (2016). Comparison of
990 radiative energy flows in observational datasets and climate modeling. *J. Appl. Meteor. Clima-*
991 *tol.*, 55, 93-117, doi:10.1175/jamc-d-14-0281.1.

992

993 Romanski, J., & Rossow, W.B. (2013). Contributions of individual atmospheric diabatic
994 heating processes to the generation of available potential energy. *J. Climate*, 26, 4244-
995 4263, doi:10.1175/jcli-d-12-00457.1.

996

997

998 Rose, F.G., Rutan, D.A., Charlock, T., Smith, G.L., & Kato, S. (2013). An algorithm for the con-
999 straining of radiative transfer calculations to CERES-observed broadband to-of-atmosphere irra-
1000 diance. *J. Atmos. Ocean. Tech.*, 30, 1091-1106, doi:10.1175/jtech-d-12-00058.1.

1001

1002 Rossow, W.B., Walker, A.W., & Garder, L.C. (1993). Comparison of ISCCP and other
1003 cloud amounts. *J. Climate*, 6, 2394-2418, doi:10.1175/1520-
1004 0442(1993)006<2394:coiaoc>2.0.co;2.

1005

1006 Rossow, W.B., & Cairns, B. (1995). Monitoring changes of clouds. *Climatic Change*, 31,
1007 305-347, doi:10.1007/978-94-011-0323-7_11.

1008

1009

1010 Rossow, W.B., & Zhang, Y-C. (1995). Calculation of surface and top-of-atmosphere radiative
1011 fluxes from physical quantities based on ISCCP datasets, Part II: Validation and first results. *J.*
1012 *Geophys. Res.*, 100, 1167-1197, doi:10.1029/94jd02746.

1013

1014 Rossow, W.B., Zhang, Y-C., & Wang, J-H. (2005). A statistical model of cloud vertical structure
1015 based on reconciling cloud layer amounts inferred from satellites and radiosonde humidity pro-
1016 files. *J. Climate*, 18, 3587-3605, doi:10.1175/jcli3479.1.

1017

1018 Rossow, W.B., & Zhang, Y-C. (2010). Evaluation of a statistical model of cloud vertical struc-
1019 ture using combined CloudSat and CALIPSO cloud layer profiles. *J. Climate*, 23, 6641-6653,
1020 doi:10.1175/2010jcli3734.1.

1021

1022 Rossow, W.B., & Ferrier, J. (2015). Evaluation of long-term calibrations of the AVHRR visible
1023 radiances. *J. Atmos. Ocean Tech.*, 32, 744-766, doi:10.1175/jtech-d-14-00134.1.

1024

1025 Rossow, W.B., Zhang, Y-C., & Tselioudis, G. (2016). Atmospheric diabatic heating in different
1026 weather states and the general circulation. *J. Climate*, 29, 1059-1065, doi:10.1175/jcli-d-15-
1027 0760.1.

1028

1029 Rossow, W.B. (2017). ISCCP H-Version – Climate Algorithm Theoretical Basis Document,
1030 NOAA Climate Data Record Program (CDRP-ATDB-0.872) Rev 0 (2017), 301 pp., Available at
1031 http://www1.ncdc.noaa.gov/pub/data/sds/cdr/CDRs/Cloud_Properties-
1032 [ISCCP/AlgorithmDescription_01B-29.pdf](http://www1.ncdc.noaa.gov/pub/data/sds/cdr/CDRs/Cloud_Properties-ISCCP/AlgorithmDescription_01B-29.pdf)

1033

1034 Rossow, W.B., Knapp, K.R., & Young, A.H. (2022). International Satellite Cloud Climatology
1035 Project: Extending the record. *J. Climate*, 35, 141-158, doi:10.1175/jcli-d-21-0157.1.

1036

1037 Rothman, L. S., & coauthors (2013). The HITRAN2012 molecular spectroscopic database, *J.*
1038 *Quantitative Spectroscopy & Radiative Transfer*, 130(2013), 4-50.

1039

1040 Stackhouse, P.W., Cox, S.J., Mikovitz, J.C., & Zhang, T. (2021). GEWEX (Global Energy and
1041 Water Exchanges Project) Surface Radiation Budget (SRB) Release 4 Integrated Product (IP4)
1042 Algorithm Theoretical Basis Document and Evaluation,
1043 https://asdc.larc.nasa.gov/documents/srb/SRB_Rel4-IP_ATBD.pdf.

1044

1045 Stephens, G.L., Wild, M., Stackhouse, P.W., L'Ecuyer, T., Kato, S., & Henderson, D.S. (2012).
1046 The global character of the flux of downward longwave radiation. *J. Climate*, 25, 2329-2340,
1047 doi:10.1175/jcli-d-11-00262.1.

1048

1049 Stephens, G.L., Hakuba, M.Z., Hawcroft, M., Haywood, J.M., Behrangi, A., Kay, J.E. et al.
1050 (2016) The curious nature of the hemispheric symmetry of the Earths' energy and water balances.
1051 *Curr. Clim. Change Rep.* (2016), 2, 135-147, doi:10.1007/s40641-016-0043-9.

1052

1053 Stephens, G.L., Hakuba, M.Z., Kato, S., Gettelman, A., Dufesne, J-J., Andrews, T., Cole, J.N.S.,
1054 Willem, U., & Mauritsen, T. (2022). The changing nature of Earth's reflected sunlight.
1055 *Proc. R. Soc. A.*, 478, 20220053, (1-16), doi:10.1098/rspa.2022.0053.

1056

1057 Stubenrauch, C., Rossow, W.B., & Kinne, S. (2012). GEWEX Assessment of Global Cloud Data
1058 Sets from Satellites. WCRP 23/2012, November, pp. 176.

1059

1060 Stubenrauch, C.J., Rossow, W.B., Kinne, S., Ackerman, S.A., Cesana, G., Chepfer, H. et
1061 al. (2013). Assessment of global cloud datasets from satellites: Project and database initi-
1062 ated by the GEWEX Radiation Panel. *Bull. Amer. Meteor. Soc.*, 94, 1031-1049,
1063 doi:10.1175/bams-d-12-00117.1.

1064

1065 Su, W., Corbett, J., Eitzen, Z., & Liang, L. (2015a). Next-generation angular distribution models
1066 for top-of-atmosphere radiative flux calculations from CERES instruments: methodology. *At-*
1067 *mos. Meas. Tech.*, 8, 611-632, doi:10.5194/amt-8-611-2015.

1068

1069 Su, W., Corbett, J., Eitzen, Z., & Liang, L. (2015b). Next-generation angular distribution models
1070 for top-of-atmosphere radiative flux calculations from CERES instruments: validation. *Atmos.*
1071 *Meas. Tech.*, 8, 3297-3313, doi:10.5194/amt-8-3297-2015.

1072

1073 Tromeur, E., & Rossow, W. B. (2010). Interaction of tropical deep convection with the large-
1074 scale circulation in the Madden-Julian oscillation. *J. Climate*, 23, 1837-1853,
1075 doi:10.1175/202009jcli3240.1.

1076

1077 Tselioudis, G., Rossow, W.B., Jakob, C., Remillard, J., Tropf, D., & Zhang, Y-C. (2021). Evalu-
1078 ation of clouds, radiation, and precipitation in CMIP6 models using global Weather States de-
1079 rived from ISCCP-H cloud property data. *J. Climate*, 34, 7311-7324, doi:10.1175/jcli-d-21-
1080 0076.1.

1081

1082 Van Den Broeke, M., Reijmer, C., Van As, D., Van De Wal, R., & Oerlemans, J. (2005). Sea-
1083 sonal cycles of Antarctic surface energy balance from automatic weather stations. *Annals Glaci-*
1084 *ology*, 41, 131-139, doi:10.3189/172756405781813168.

1085

1086 Wang, J., Rossow, W.B., & Zhang, Y-C. (2000). Cloud vertical structure and its varia-
1087 tions from a 20-year global rawinsonde dataset. *J. Climate*, 13, 3041-3056,
1088 doi:10.1175/1520-0442(2000)013<3041:cvsai>2.0.co;2.

1089

1090 Wielicki, B.A., Wong, T., Allan, R.P., Slingo, A., Kiehl, J.T., Soden, B.J., et al. (2002). Evi-
1091 dence for large decadal variability in the tropical mean radiative energy budget. *Science*, 295,
1092 841-844, doi:10.1126/science.1065837.

1093

1094 Wild, M., Gilgen, H., Roesch, A., Ohmura, A., Long, C.N., Dutton, E.G., et al. (2005). From
1095 dimming to brightening: Decadal changes in solar radiation at Earth's surface. *Science*, 308, 847-
1096 850, doi:10.1126/science.1103215.

1097

1098 Wild, M. (2009). Global dimming and brightening: A review. *J. Geophys. Res.*, 114, D00D16,
1099 (1-31), doi:10.1029/2008jd011470.

1100

1101 Wild, M., Hakuba, M.Z., Folini, D., Dorig-Ott, P., Schar, C., Kato, S., & Long, C. (2018). The
1102 cloud-free global energy balance and inferred cloud radiative effects: an assessment based on
1103 direct observations and climate models. *Climate Dynamics*, 52, 4787-4812, (1-26),
1104 doi:10.1007/s00382-018-4413y.

1105

- 1106 Wong, T., Wielicki, B.A., Lee, R.B., Smith, G.L., Bush, K.A., & Willis, J.K. (2006). Reexami-
1107 nation of the observed decadal variability of the Earth radiation budget using altitude-corrected
1108 ERBE/ERBS nonscanner WFOV data. *J. Climate*, 19, 4028-4040. doi:10.1175/jcli3838.1.
1109
- 1110 Young, A.H., Knapp, K.R., Inamdar, A., Hankins, W., & Rossow, W.B. (2018). The Internation-
1111 al Satellite Cloud Climatology Project H-Series Climate Data Record Product. *Earth System Sci-*
1112 *ence Data*, 10, 583-593, doi:10.5194/essd-10-583-2018.
1113
- 1114 Zhang, Y-C., Rossow, W.B., & Lacis, A.A. (1995). Calculation of surface and top of atmosphere
1115 radiative fluxes from physical quantities based on ISCCP datasets 1. Method and sensitivity to
1116 input data uncertainties. *J. Geophys. Res.*, 100, 1149-1165, doi:10.1029/94jd02747.
1117
- 1118 Zhang, Y-C., & Rossow, W.B. (1997). Estimating meridional energy transports by the atmos-
1119 pheric and oceanic general circulations using boundary fluxes. *J. Climate*, 10, 2358-2373,
1120 doi:10.1175/1520-0442(1997)010<2358:emetbt>2.0.co;2.
1121
- 1122 Zhang, Y-C., Rossow, W.B., Lacis, A.A. Oinas, V., & Mishchenko, M. I. (2004). Calculation of
1123 radiative fluxes from the surface to top of atmosphere based on ISCCP and other global data sets:
1124 Refinements of the radiative transfer model and the input data. *J. Geophys. Res.*, 109, D19105,
1125 (1-27), doi:10.1029/2003jd004457.
1126

1127 Zhang, Y., Rossow, W.B., & Stackhouse, P.W. (2006). Comparison of different global infor-
1128 mation sources used in surface radiative flux calculation: Radiative properties of the near-surface
1129 atmosphere. *J. Geophys. Res.*, 111, D13106, (1-13), doi:10.1029/2005jd006873.

1130

1131 Zhang, Y-C., Rossow, W.B., & Stackhouse, P.W. (2007). Comparison of different global infor-
1132 mation sources used in surface radiative flux calculation: Radiative properties of the surface. *J.*
1133 *Geophys. Res.*, 112, D01102, (1-20), doi:10.1029/2005jd007008.

1134

1135 Zhang, Y-C., Rossow, W.B., Long, C.N., & Dutton, E.G. (2010). Exploiting diurnal variations to
1136 evaluate the ISCCP-FD flux calculations and Radiative-Flux-Analysis-Processed Surface Obser-
1137 vations from BSRN, ARM and SURFRAD. *J. Geophys. Res.*, 115, D15105, (1-21),

1138 doi:10.1029/2009jd012743.

1139

1140 Zhang, Y-C. (2017). ISCCP-FH Radiative Flux Profile Product, Climate Algorithm Theoretical
1141 Basis Document (C-ATBD), NOAA NCEI Climate Data Record (CDR) Program, 2017,
1142 https://isccp.giss.nasa.gov/pub/flux-fh/docs/C-ATBD_ISCCP-FH.pdf, through login to
1143 <https://isccp.giss.nasa.gov/projects/flux.html>.

1144

1145 **Table 1.** Differences of monthly mean ISCCP-FH and FD TOA fluxes with CERES (Edition 3A,
 1146 CERES Science Team, 2013) and SRF fluxes with BSRN (Ohmura et al., 1998) in Wm^{-2} for
 1147 2007. The statistics include spatial variability over location at 110 km scale as well as month-to-
 1148 month variability. The uncertainty range is based on the normal deviations (rms with bias re-
 1149 moved) (cf. Rossow and Zhang, 1995).

TOA		
	FH minus CERES	FD minus CERES
SWnet	-7 ± 6	-8 ± 6
Correlation for SWnet	0.99	0.99
LWnet	$+7 \pm 3$	$+3 \pm 3$
Correlation for LWnet	0.99	0.99
Overall uncertainty	≤ 10	≤ 10
Surface		
	FH minus BSRN	FD minus BSRN
SWnet	-1 ± 15	-4 ± 17
Correlation for SWnet	0.99	0.99
LWnet	-7 ± 12	$+10 \pm 14$
Correlation for LWnet	0.97	0.97
Overall uncertainty	≤ 15	≤ 20

1150

1151 **Table 2.** Evolution of flux biases (Wm^{-2}) from comparisons with spatially matched ERBE or
 1152 CERES at top-of-atmosphere and GEBA (Wild et al. 2017) or BSRN at surface (Driemel et al.
 1153 2018)†.

	TOA		
	FC – ERBE	FD – ERBE	FH – CERES
SWup	+10.7	+4.7	+7.2 (+7.5, +5.0)
LWup	-1.1	-2.2	-7.1 (-7.0, -8.0)
Net	-9.3	-2.0	0.0 (-0.5, -3.2)
	Surface		
	FC – GEBA	FD – BSRN	FH – BSRN
SWdn	+15.2	+2.0	-1.4
LWdn	-19.4	+2.2	-7.5
Net	N/A	N/A	(+4.1)

1154 †The FC comparisons are based on 16 seasonal months over 1985 – 1989 as reported in Rossow
 1155 et al. (1995). The FD comparison with ERBE is also based on the same 16 seasonal months as
 1156 FC but the FD comparison with BSRN is based on all months over 1992 – 2001 as reported in
 1157 Zhang et al. (2004). The FH comparisons are based on monthly means in 2007 from CERES
 1158 (SYN1deg Ed3a) and BSRN; values in parentheses represent the bias with respect to CERES
 1159 SYN1deg 4.1 for 2007–2009 period and EBAF 4.1 for 2001–2009 period, respectively, cited
 1160 from Stackhouse et al. (2021).
 1161

1162 **Table 3.** (First three numerical columns) Comparison of global-time-average flux results for 16
 1163 mid-seasonal months for the same four year period (April 1985 to January 1989) from the three
 1164 versions of calculations (all are in Wm^{-2} except albedo in %) and (Rightmost column) mean
 1165 (standard deviation) of 1° -equal-area maps over all the monthly means from July 1983 to June
 1166 2017^a.

Quantity	FC	FD	FH	34-year FH
TOA				
SWdn	341.6	341.8	340.3	340.4 (130.9)
SWup	111.5	105.6	104.6	104.5 (50.6)
LWup	234.2	233.2	231.5	232.3 (32.8)
SWnet	230.1	236.3	235.7	236.1 (107.1)
LWnet	-234.2	-233.2	-231.5	-232.3 (32.8)
NET	-4.1	3.1	4.2	3.8 (88.3)
SWcre	-53.7	-50.4	-49.0	-48.8 (33.8)
LWcre	21.3	26.2	28.3	26.9 (15.4)
Albedo	32.6	30.9	30.7	30.7 (13.8)
Atmosphere				
SWnet	65.0	70.8	77.4	77.0 (30.5)
LWnet	-188.4	-182.0	-179.8	-178.9 (37.6)
NET	-123.4	-111.2	-102.5	-101.9 (33.2)
SWcre	-1.6	2.9	2.5	2.6 (3.5)
LWcre	-3.6	-3.1	7.1	5.4 (20.8)
Surface				
SWdn	193.4	189.4	183.4	183.9 (84.2)
SWup	28.3	24.0	25.1	24.8 (35.2)
LWdn	348.3	344.6	346.0	340.9 (76.1)
LWup	394.1	395.7	397.6	394.3 (75.6)
SWnet	165.1	165.4	158.3	159.1 (80.3)
LWnet	-45.8	-51.1	-51.6	-53.4 (25.7)
NET	119.3	114.3	106.7	105.7 (83.5)
SWcre	-52.2	-53.3	-51.5	-51.5 (36.0)
LWcre	24.9	29.3	21.2	21.5 (15.3)
Albedo	14.6	12.7	13.7	13.5 (18.6)

1167 ^aCloud Radiative Effect (CRE as used in this table in SWcre and LWcre for SW and LW,
 1168 respectively) is for net fluxes, positive sign means radiative heating in the system (the earth-
 1169 atmosphere, earth or atmosphere system for TOA, surface or atmosphere) as conventionally
 1170 defined. The original FH 1° -equal-area map is re-gridded to the same 2.5° -equal-area map as FC
 1171 and FD before averaging for the 16-month comparison. Albedo for both TOA and SRF are
 1172 calculated based on averaged SWup and SWdn (because albedo is the ratio of SWup to SWdn
 1173 that cannot be linearly averaged); however, the standard deviation for Albedo is based on all
 1174 monthly mean albedo values (like all other parameters) for a reference.

1175

1176

1177 **Table 4.** Mean Net Fluxes and Cloud Radiative Effects at TOA, at Surface and in Atmosphere
 1178 for 1998 to 2002 and 2008 to 2012 periods in Wm^{-2} .

	SWnet	LWnet	Net	SWcre	LWcre	NETcre
	TOA					
1998-2002 mean	237.1	-232.8	4.3	-48.0	26.3	-21.7
2008-2012 mean	235.5	-232.0	3.5	-49.8	26.8	-22.9
	Surface					
1998-2002 mean	160.3	-53.4	107.0	-50.6	21.6	-29.0
2008-2012 mean	158.8	-53.5	105.3	-52.4	21.6	-30.8
	Atmosphere					
1998-2002 mean	76.8	-179.4	-102.6	2.6	4.7	7.3
2008-2012 mean	76.8	-178.5	-101.8	2.7	5.2	7.9